Starspot regions die without aging from G dwarfs to the fully convective boundary

Matthew D. Schwartz*
Department of Physics, Harvard University

Cecilia Garraffo
AstroAI, Center for Astrophysics | Harvard & Smithsonian

Abstract

Whether an old starspot is closer to death than a young one of the same size has so far been answered only for the Sun: in a companion paper we followed sunspot groups individually through a century and a half of daily records and found that a group's death rate at fixed size rises with age. On other stars, outside a handful of Doppler and transit maps, spots are seen only through the recurring dips in brightness they produce as the star rotates, and a single dip may come from many spots. We call a dip followed from one rotation to the next a spot feature; so far only the decay timescales of such features have been measured. A timescale cannot say whether the risk of death depends on age. These lifetimes matter well beyond the spots: the evolution of active regions sets the timescale of the stellar signals that hide small planets in radial velocities and transit photometry, light-curve models leave the lifetime unconstrained, and a death rate that rose with age would reveal an internal clock in the magnetic structure. We find that on 509 heavily spotted Kepler and TESS dwarfs these spot features die without aging. At fixed birth depth, within a single star, an old feature is no likelier to die than a young one. We followed 10,051 features from birth to death; 6,359 of them, and 158 more on eight further stars of the G–K core sample, enter the survival fits on 260 stars. On G and K dwarfs a log death rate rising by 0.05 per rotation would have been detected. We measure median completed lifetimes of four to five rotations in every sample and Kaplan–Meier medians of five to seven, with longer lifetimes compressed because our tracking cannot follow a feature much beyond six or seven rotations. The lifetimes scale in days as $P^{0.828}$ with the rotation period P, and the Rossby number fits less closely for five turnover times tested. No aging is detected on the early-M dwarfs either, where the bound is weaker, and their lifetimes also rise with the rotation period. Past the fully convective boundary the smaller TESS sample shows a flat hazard and tracked lifetimes proportional to the period, but its simulations can neither bound aging nor distinguish a lifetime fixed in days from one fixed in rotations. On the early-M dwarfs new features appear at recently dead sites more often than on G–K light curves degraded to the same sensitivity, after allowing for chance coincidences on each. The Sun itself would not enter such a sample, since its rotational variability lies below the selection cut. Modeled as a Kepler target from its full sunspot-group record, it yields fewer than two trackable features per year of solar maximum and at most 13 in any four-year window, against the fifty a survival fit needs. The flat stellar hazard does not contradict the solar result: a light-curve feature is an active site where spot groups keep emerging, and in a model of such sites, once a steadily fed site is older than one to two lifetimes of its member groups, it dies at a rate independent of its

*Work done with Anthropic, but results and views are not endorsed by Anthropic.

age, however those groups age. No feeding configuration we tested, however, reproduces the flat hazard together with the observed lifetimes and depths.

1 Introduction

Solar observers have drawn sunspots and sunspot groups every day for a century and a half, so on the Sun a spot or a group can be followed from birth to death whenever both happen on the visible disk. On other stars neither spots nor groups are resolved: the star dims each time a dark region rotates across its disk, and one dip usually blends several spots or groups at neighboring longitudes. We therefore work with light-curve features, a feature being a dip that we follow from one rotation to the next until it fails to return, most likely a group or complex of starspots at one longitude rather than a single spot. For these features we ask whether an old one is nearer death than a young one of the same depth, what clock sets its lifetime, and whether the answers change from G dwarfs down to the smallest spotted dwarfs.

The decay laws, the rules for how fast a sunspot's area shrinks, fitted to a century of solar area records disagree by a factor of four. Martínez Pillet et al. (1993) draw each spot's decay rate from a lognormal distribution and hold it fixed, Petrovay and van Driel-Gesztelyi (1997) set the rate by the spot's current size, and Bradshaw and Hartigan (2014) by erosion in the surrounding turbulence. In a companion paper (Schwartz and Garraffo, 2026) we measured the solar death law itself on the 25,883 USAF/NOAA sunspot-group histories observed from birth. At fixed current area and fixed per-group hardiness, the risk of dying rises with age, at +0.184 per day in log hazard, so individual sunspot groups age.

Giles et al. (2017) measured the decay timescale of the modulation as a whole from the autocorrelation of Kepler light curves and mapped its run with light-curve amplitude and spectral type. Basri and Nguyen (2018) built morphology statistics of the dips, and Basri et al. (2022) calibrated lifetimes from the decay of autocorrelation peak heights. Santos et al. (2021) applied the autocorrelation estimator to simulated light curves of known spot lifetime and recovered about half of the input lifetime. In their review, Işık et al. (2026) list empirical lifetime distributions as a function of spectral type, which on unresolved stars can only be distributions of feature lifetimes, among the measurements still missing. They call these distributions essential if transit mapping is to become a reliable surface diagnostic across the cool-star sequence.

A few studies have also followed individual features of this kind through their lives, in photometric dips rather than resolved images. Hall and Busby (1990) compared the lifetimes of 40 spots on 17 stars with what differential-rotation shear would allow, and Hall and Henry (1994) considered 112 starspots on 26 spotted stars from ground-based photometry. Namekata et al. (2019, 2020) tracked individual dips through consecutive rotations on Sun-like Kepler stars and found the lifetimes of their 56 spots rising with the rotation period. A timescale does not determine whether the risk of death depends on age. Two death laws with the same mean lifetime can have different hazard shapes, and the shape distinguishes features that wear out from features that die at random.

Skumanich (1972) showed that rotation and activity decline together as stars spin down, and activity tracks rotation most tightly through the Rossby number, the rotation period divided by the convective turnover time (Noyes et al., 1984; Wright et al., 2011). The rotation–activity relation continues unbroken across the fully convective boundary (Wright et al., 2018), and empirical tables of convective turnover time now extend down the low-mass main sequence (Gossage et al., 2025). Whether a feature lifetime keeps rotation time or Rossby time is therefore a physical question rather than a choice of units.

In this paper, we measure the risk that a feature dies in its next rotation as a function of its age. The answers matter beyond the spots themselves: the lifetime of active regions sets the timescale of the correlated activity signals that limit the detection of small planets in radial velocities and photometry (Dumusque et al., 2011; Haywood et al., 2014; Rajpaul et al., 2015), and forward models of stellar light curves leave that lifetime unconstrained and degenerate with the degree of nesting (Nèmec et al., 2023; Sowmya et al., 2022). A death rate that rises with age, as on the Sun, would also mean that whatever destroys a feature keeps an internal clock, while a flat one is what memoryless erosion or steady replenishment would give. We study whether the death of these features depends on age, as that of the Sun's groups does; what clock their lifetimes keep; whether the rules change from G dwarfs to the fully convective boundary; and, if the stars' features do not age while the Sun's groups do, what reconciles the two. We tracked roughly ten thousand features, rotation by rotation, on 509 of the 516 dwarfs we selected, G–K and early-M dwarfs over four years of Kepler photometry and stars at and past the fully convective boundary in TESS.

Section 2 describes the samples, the dip tracking and censoring rules, and the survival models with their calibration by injection. Section 3 takes the questions in turn, and Section 4 draws the consequences for how a light-curve feature relates to the spot groups beneath it.

2 Data and methods

As in the companion solar paper (Schwartz and Garraffo, 2026), we treat the death of a tracked feature as a censored event in the sense of survival analysis (Kaplan and Meier, 1958; Cox, 1972). A censored history is one that ends while the feature still exists (is still alive, in the demographers' language), because the observations stop or a gap begins; it says only that the feature lasted at least that long, and we keep that lower limit instead of discarding the history or counting it as a death, as astronomers do with upper limits (Feigelson and Nelson, 1985). The hazard is the death rate per rotation among the features still alive at a given age, which at the small values found here is close to the fraction of them that die in the next rotation. We follow each feature from its first sighting and fit that per-rotation hazard against age, and a censored history contributes only the rotations over which we watched it (Section 2.2).

2.1 Stellar samples and the solar registry

We analyze three samples of heavily spotted dwarfs, 516 selected stars of which 509 carry the 10,051 tracked features, and the Sun's daily record of sunspot groups (Table 1, Appendix F). The Sun's record, the fourth row of Table 1, is the registry of 25,883 sunspot group histories observed from birth, spanning 1874–2025, on which we measured the death law of sunspot groups in the companion solar study (Schwartz and Garraffo, 2026).

The primary sample contains 249 G–K dwarfs selected from the 34,030-star rotation-period catalog of McQuillan et al. (2014), with effective temperatures and surface gravities from the Kepler DR25 catalog (Mathur et al., 2017). We kept dwarfs ($\log g \geq 4.2$) with secure rotation periods ($P_{\rm rot}$ = 5–15 d, fractional period uncertainty of 2% or less, catalog weight $w \geq 0.5$), bright enough for clean photometry (Kepler magnitude $K_p < 13.5$), and heavily spotted. We required the catalog's per-rotation variability range $R_{\rm per} \geq 5{,}000$ parts per million (ppm) of the star's flux, because only heavily spotted stars keep features above threshold long enough for us to observe their deaths. We

Table 1: Stellar samples and the solar registry. Columns give the number of stars, the effective-temperature and rotation-period ranges, the numbers of tracked features and of interval-censored deaths under the rules of Section 2.2, and the catalog that supplied targets and rotation periods.

Sample	Stars	$T_{\rm eff}$ [K]	$P_{\rm rot}$ [d]	Features	Deaths	Source
Kepler G–K dwarfs	249	3900–6000	5–15	4,954	4,092	McQuillan et al. (2014)
Kepler early-M dwarfs	230	3300–3900	5–45	2,875	2,305	McQuillan et al. (2014)
TESS fully convective	37	2994–3292	1.1–12.5	2,222	1,568	Stassun et al. (2019)
Sun (group registry)	1	...	...	25,883	...	Schwartz and Garraffo (2026)

then ranked the stars by $R_{\rm per}$ inside five temperature bins spanning 3900–6000 K and took them from the top of each bin. Over the four-year Kepler baseline, 242 of the 249 selected stars gave 4,954 tracked features and 4,092 deaths, and the 225 with at least ten features enter the per-bin survival fits of Section 3.1. The pooled fit of Table 2 and the calibration of Section 2.4 use a core sample of 100 G–K stars at 3900–5400 K that pass the same cuts and carry 2,054 tracked features. We ranked these 100 stars by $R_{\rm per}$ over 3900–5400 K without binning, so 92 of them are among the 249 selected stars and 8, all in the 4900–5400 K bin, fall below that bin's rank cutoff in the 249-star selection. The 89 core stars with at least ten features each, and their 1,988 features, form the fitted subsample of Table 2. All 8 stars outside the selection are among these 89, with 158 of the 1,988 features, and the pooled fit does not depend on them (Section 3.1).

We applied the same selection to the early-M sample, 230 dwarfs with $3300 \leq T_{\rm eff} < 3900$ K (spectral types M0–M3), rotation periods of 5–45 d, and $K_p < 16$. For these fainter stars the amplitude cut scales with magnitude, $R_{\rm per} \geq 5{,}000 \times \max\left(1, 10^{\,0.2(K_p-13.5)}\right)$ ppm, so a fainter star must be proportionally more spotted to enter.

The fully convective sample comes from TESS (Ricker et al., 2015). Of 40 candidate stars past the fully convective boundary selected from the TESS Input Catalog (Stassun et al., 2019), 37 have at least one contiguous run of 6 to 14 consecutive sectors, long enough to track features across rotations, and we analyze each such run as one light curve. These 37 stars span TIC temperatures of 2994–3292 K, roughly M3.5–M5. On the 2-minute-cadence SPOC PDCSAP light curves (720 cadences per day in every run), their 72 runs total 6,283 rotations and give 2,222 tracked features, 1,568 of them ending in an observed death.

2.2 Dip tracking and censoring

A tracked feature is one dip followed from rotation to rotation at the same rotational phase. Physically it is a dark region at one longitude of the star that stays above the detection threshold, in general several spots or whole groups blended together rather than a single spot, and we interpret it as an active site fed by repeated flux emergence (Section 3.8). We read a feature's life and death directly from the light curve. It lives while its dip returns at the same rotational phase every rotation, and it dies when we observe that phase and find no dip. We applied the same detection, tracking, and censoring rules to the three samples. For detection we use the PDCSAP long-cadence photometry, median-normalized per quarter, and measure each dip's depth against a rolling 95th-percentile envelope of width $2\,P_{\rm rot}$. A dip counts as detected when its depth exceeds $\max(5\sigma_{\rm smooth}, 1{,}000\ \mathrm{ppm})$, where $\sigma_{\rm smooth}$ is the star's smoothed photometric noise, so the threshold is 1,000 parts per million or five times that noise, whichever is larger. Distinct dips must lie at least

$0.08\,P_{\rm rot}$ apart in phase.

We joined dips into feature histories by phase continuity. A new dip extends an existing track when its phase lies within a circular offset $|\Delta\phi| \leq 0.08$ of the track's running phase, an exponentially weighted mean with weight $\alpha = 0.3$, and when several dips and tracks compete, we match the closest pair first, one to one. We confirmed a track as a feature only if we sighted it at least twice within its first three rotations, so a feature enters the sample at the age of its second sighting. The earliest possible death is therefore at age 2, the first age at which we measure the death hazard. A rotation counts as observed for a track only when at least half of the expected cadences within $\pm 0.08\,P_{\rm rot}$ of the predicted crossing are present, so a gap in the data is never recorded as a death.

We count a feature as dead only after two consecutive observed rotations without a matching dip; the death is then interval-censored, known only to lie between the last matched rotation and the second empty one. If instead the feature's predicted phase is unobservable for three consecutive rotations (quarter gaps, safe modes, monthly downlinks), or the baseline ends, we close the history as censored at its last match. When two confirmed tracks approach within $\Delta\phi < 0.06$ we censor both, because their identities have become ambiguous and keeping the deeper of the two would select on depth. We exclude outright any feature already present at the start of observability, because its birth age is unknown and the likelihood of Section 2.3 depends on ages counted from birth. When a feature dies at phase p and a new confirmed feature is born within three rotations at a circular offset $|\Delta\phi| \leq 0.08$ of p, we mark the pair during tracking as a site recurrence, a fresh feature at the site of a dead one.

2.3 Survival models with a shared frailty per star

For each tracked feature i on star s we model the death hazard $\lambda_i(a)$ at age a, counted in rotations since birth, as the exponential of a sum of terms,

$$\log \lambda_i(a) \;=\; \beta_0 + \beta_d \ln(1 + d_i/d_0) + g(a), \qquad g(a) \;=\; \begin{cases} 0 & \text{memoryless,} \\ B\,a & \text{Gompertz,} \\ B_{\ln} \ln(1+a) & \text{Weibull-type,} \end{cases} \tag{1}$$

where d_i is the depth of the feature's dip at its first matched sighting (its depth at birth), $d_0 =$ 100 ppm sets the depth scale, and $g(a)$ is the age term, whose three forms are the three models we compare. Age advances in whole rotations, so $\lambda_i(a)$ is the hazard integrated over rotation a, and a feature alive at the start of that rotation dies during it with probability $1 - e^{-z\lambda_i(a)}$ given its star's frailty z, defined below. The memoryless model has no age dependence, so an old feature is at no more risk than a young one. In the Gompertz model the log hazard is linear in age and rises by the Gompertz slope B with each rotation, so that the hazard is multiplied by e^B from one rotation to the next. In the Weibull-type model the log hazard is linear in the logarithm of age. We rank the models by their Akaike information criterion (AIC), and we judge every ΔAIC against the distribution that simulations without aging produce through the same analysis (Section 2.4). We condition the hazard on depth at birth rather than on current depth, because a feature grows shallower as it decays, so a fit on current depth would assign part of any age dependence to the depth coefficient β_d instead of to the age term $g(a)$. For comparison with the solar fit, which holds a group's current area fixed, Section 3.1 also reports these fits with the depth at each sighting as the covariate.

Stars differ in unobserved properties that set how long their features last, such as the rate of spot emergence and the surface shear, and a population fit that ignores these differences confounds the heterogeneity with aging. The features on high-hazard stars die first, so the survivors at any age come increasingly from low-hazard stars and the population hazard declines with age even when no individual feature ages. We absorb the heterogeneity with a frailty term, a multiplier z on the hazard that stands for those fixed properties of the star and is shared by all its features. The multiplier is gamma-distributed with mean one and variance σ^2, so that a feature with cumulative hazard Λ has marginal survival $\mathbb{E}_z[e^{-z\Lambda}] = (1+\sigma^2\Lambda)^{-1/\sigma^2}$. The likelihood of star s, used by every fit in this paper, is

$$\mathcal{L}_s \;=\; \frac{\mathbb{E}_z\big[\prod_{i\in s} P_i(z)\big]}{\mathbb{E}_z\Big[\,e^{-z\sum_{i\in s}\Lambda_i(t_i)}\Big]}, \qquad P_i(z) \;=\; \begin{cases} e^{-z\Lambda_i(L_i)} - e^{-z\Lambda_i(R_i)} & \text{death bracketed in } (L_i, R_i], \\ e^{-z\Lambda_i(C_i)} & \text{censored at } C_i, \end{cases} \tag{2}$$

where $\Lambda_i(a)$ is the cumulative hazard accumulated from Equation 1, the interval $(L_i, R_i]$ brackets an observed death, C_i is the age at which a censored history closes, and t_i is the age at which the feature entered the sample. Here L_i is the last rotation with a matched dip and R_i the second consecutive observed rotation without one, so the death factor is the probability that the dip was first absent in one of the rotations $L_i{+}1, \ldots, R_i$. About three quarters of the death intervals span the minimum two rotations and the rest three to six, where unobservable rotations intervene. Blends close 5.6%, 5.6%, and 8.2% of the tracked histories in the G–K core, early-M, and fully convective samples. The likelihood assumes that, given the star's frailty and each feature's depth at birth, the features of a star are independent, and that closure at a data gap, a blend, or the end of the baseline carries no information about the remaining lifetime. The denominator conditions every feature on survival to the rotation of its confirming sighting, which is what the confirmation rule selects on. That rotation then counts toward the feature's time at risk although no death can be recorded in it. The simulated populations of Section 2.4 pass through the same tracking and share this convention, so every comparison between the data and those simulations contains it on both sides.

Sharing one frailty across all the features of a star makes the star-to-star part of the heterogeneity identifiable, because the repeated features on a star fix σ^2 from the correlation among their lifetimes. This term does not absorb heterogeneity among the features of one star beyond their depth at birth, which lowers rather than raises a fitted slope just as the star-to-star heterogeneity described above does. Nor does it absorb changes in a star's activity over the baseline. A nested fit with a second, per-feature frailty is not identified on these data. Without an age term its per-feature variance goes to zero, and with one the maximum of the likelihood moves to a very large per-feature variance and a slope near 9 per rotation. Simulated populations with no aging and one lifetime law per star drive the same fit to the same place, with an even larger gain in likelihood. Adding as a covariate each feature's birth epoch, the crowding at its birth, the local detection rate, or a depth–age interaction leaves the fitted G–K age slope between 0.0048 and 0.0057 per rotation, against 0.0056 without them (Section 3.1). A separate frailty for each half of a star's baseline or for each of its Kepler years, which can follow slow changes in activity, gives 0.0066 and 0.0077, and a free intercept per star gives 0.0138. Each value lies inside the range that the same fit returns on four simulated populations without aging (up to 0.013, or 0.021 with free intercepts) and below its value on each of four populations injected at $B = 0.05$ (0.022 or more). Beyond these checks, heterogeneity within a star and changes in activity are bounded only through the injection tests of Section 2.4, so the bound on aging is conditional on heterogeneity acting between stars and through depth at birth.

We then profile the likelihood in B, maximizing over the other parameters at each value of B, and the profile has a single peak over the full interval $[-0.5, 1.5]$, away from its edges.

2.4 Calibration by injection

As a sensitivity test, we injected aging at $B = 0.02$ to 1.53 per rotation into simulated G–K populations in the forward model described below and passed them through the same detection, tracking, and fit as the data. The largest value is solar-strength aging at the core sample's median rotation period of 8.3 d. The simulated features end their lives with one of three depth profiles, a gradual fade, an abrupt shutdown, or a depth-dependent mixture of the two. We also injected a slightly declining hazard, $B = -0.01$ and -0.02 per rotation, in 15 populations per value and profile. We count injected aging as detected in a simulated population when the aging model fits a positive slope and gains more in AIC than 95% of 100 simulated populations without aging that share its end-of-life profile (described below). Of the 30 populations injected at $B = 0.05$ with each profile, we detect aging in 30, 28, and 30 for the fade, the shutdown, and the mixture, and in at least as many at every larger injected value. On the G–K sample, therefore, aging of 0.05 per rotation or more would have been detected with a probability of 0.9 or higher, however features end their lives. Against the 99th percentile instead, that statement holds from $B = 0.08$, and solar-strength aging is detected in all 30 populations of every profile under either threshold. Only about a third of the deaths that the tracking records in the simulations without aging are physical disappearances. The rest are features that dropped below threshold for two rotations while still present (43–51%, depending on the profile) or drifted out of the phase window (19–24%). An injected slope is therefore recovered attenuated, to a median of about 0.02 over the simulated populations at $B = 0.05$, and that median saturates between about 0.04 and 0.07 per rotation however large the injected value. We use these fits to detect aging, not to measure its strength, and judge every measured slope and AIC gain against injections passed through the same tracking rather than against nominal values.

We calibrate every comparison between hazard models against simulated populations without aging passed through the same analysis as the data. A parametric bootstrap that draws survival times from the fitted law on the real histories cannot calibrate these fits. The tracked records place each death at the start of an interval of two or more rotations and never in the rotation of the confirming sighting, and only synthetic light curves passed through the same tracking reproduce those conventions. In the forward model we placed synthetic spot populations with known survival laws on the observed time grids of each sample's own stars, with each star's gaps, rotation period, and measured noise. These are the 100 stars of the G–K core sample of Section 2.1, the 230 early-M stars, and the 72 TESS light curves. We calibrated the birth rates, lifetimes, and peak-depth distributions of these populations from the tracked sample, and then ran the synthetic light curves through the same detection, tracking, and fitting steps as the data. For each sample we built 300 such populations without aging, 100 for each end-of-life profile, matched in size to the real fitted sample (on early M by random thinning of the tracked features). Their distributions of $\hat{B}$ and ΔAIC are the reference against which we judge the fits in Table 2.

On the early-M light curves only about half of the simulated features that enter these fits begin at an injected spot (0.51 to 0.55 across the three profiles, against 0.93 to 0.94 on G–K). The rest are noise dips that the tracking links into features. The same light curves with no spots injected still yield tracked features, with a positive fitted slope. The 95th percentile of ΔAIC depends on the profile, from 7.9 to 14.0 on G–K and from 6.4 to 12.4 on early M. Table 2 lists the values pooled over the three profiles, and every fitted ΔAIC also lies below the lowest per-profile percentile. The data do not tell us which profile applies. Under a comparison fixed in advance, the depths of real features over the rotations before their last detection single out none of the three simulated profiles in any sample. On the early-M and fully convective samples those depths fall outside all three simulated profiles. We therefore quote, for each sample, the bound that holds for every profile. The synthetic features enter and leave the sample under the same confirmation, gap, blend, and edge rules as the real ones, with ages counted from first detection rather than from physical emergence. The reference distributions and the recovered slopes therefore include the entry selection, the censoring, and the difference between losing a dip and losing the spot. In the G–K simulations without aging the tracking first detects a spot a median of one rotation after it emerges, and records about one detected spot in five as more than one feature. The recorded death of a spot's last feature precedes the disappearance of the spot itself by a median of one rotation. Over all recorded feature deaths, which include features that end while their spot is still present, the median lead is two to three rotations. On the fully convective sample the simulated populations are a quarter smaller than the real one, and the tracking does not preserve the identity of simulated features on those crowded light curves (Appendix B). We therefore list that sample's simulations without using them as a bound.

We also re-tracked the three samples and their simulated populations, with and without aging, under twelve variants of the tracking rules of Section 2.2, thirteen sets of rules in all (Appendix E). Ten variants change one rule and two change the phase tolerance together with the miss rule. The G–K result holds under the adopted rules and ten of the twelve variants and fails only when the phase tolerance for a match is tightened from 0.08 to 0.06 rotation (Appendix E). Treating every blended history as a death at the blend instead of as censored lowers the G–K slope from 0.0056 to 0.0022.

2.5 Matched sensitivity and the within-star permutation test

The early-M stars are fainter and their features shallower relative to threshold. Before matching, a flat hazard measured on the early-M sample therefore places a weaker limit on aging than the same flat hazard on the G–K sample, and any rate statistic could differ between the classes from the unequal sensitivity rather than from a physical difference between the stars. We detect dips in both samples with the same threshold rule, including its minimum of 1,000 parts per million. The two samples differ in how high each star's detection threshold lies relative to the depths of its dips, which we measure by the ratio

$$\rho_s \;=\; \frac{\tau_s}{D_s}, \tag{3}$$

where τ_s is the star's detection threshold and D_s is the median peak depth of its tracked features. The median of ρ_s is 1.37 times larger on the early-M sample than on the G–K sample, and the difference grows in the upper tail of the ρ_s distribution. We matched the two samples by adding noise to the real G–K light curves, degrading them to early-M sensitivity, because added noise worsens detection, tracking, and depth measurement together, as happens physically on fainter, redder stars. We repeated the detection, tracking, and survival fits on the degraded light curves of all 100 stars of the G–K core sample. The degraded G–K sample and the early-M sample then have median ρ in a ratio of 1.112, within the 0.12 deviation from unity that we set as the condition for a match.

We compare the two classes through one statistic, the rate of site recurrences, which are deaths followed within three rotations by a birth at the same phase under the pairing rule of Section 2.2. A crowded surface produces coincidences by chance, so the reference value for this statistic is the number of recurrences expected from the star's own feature counts and birth phases. We estimate that number with the occupancy null, a permutation test within each star. We permuted the birth phases among the star's own tracks, which changed only the positions and kept each star's feature counts, depth series, durations, birth and death rotations, and censoring types, and recomputed the recurrence statistic with the same pairing rule. The permutation keeps each star's set of birth phases and each track's phase drift and removes only the link between where one feature died and where the next was born. A second null that redraws every birth phase uniformly gives rates within 0.3 percentage points of the first on both samples, so the comparison does not depend on that choice. Neither null accounts for a feature that the tracking loses and later recovers, which re-enters as a birth where another died (Section 3.2), or for the room in rotational phase that a death frees for new detections on a crowded star. An excess over the null therefore does not by itself measure physical re-emergence, and we compare it instead with the excess on G–K light curves degraded to early-M sensitivity (Section 3.4). To measure how well this statistic recovers real recurrences, we gave 10% of each star's deaths a forced coincident birth on permuted positions, and recovered the injected coincidences at a mean net rate of 0.666 on G–K and 0.622 on early-M. The net rate is the increase in recurrences counted by the pairing rule over the same permuted data without the injections, divided by the number injected.

3 Results

We find that in all three samples the death hazard of a tracked feature is flat in age once we hold star-level frailty and depth at birth fixed, that is, the probability that a feature disappears in its next rotation depends on its depth at birth and on its star but not on how many rotations it has already lived; in the demographers' language, the features die without aging (Section 3.1, Table 2). In neither Kepler sample does the aging model gain more in AIC, or fit a larger positive slope, than in 95% of the simulated populations without aging passed through the same detection, tracking, and fit (Table 2). For lifetimes inside the tracking window, below about 60 d at these periods, the lifetime of a feature is set in rotations (Section 3.2). The tracked lifetimes scale with the rotation period of the star, which fits them more tightly than the Rossby number does for each of the five turnover times tested (Section 3.3). The early-M and fully convective samples also show no aging and lifetimes that rise with the period, though the early-M bound on aging is weaker and the fully convective sample gives none (Sections 3.4 and 3.5, Appendix B). After allowing for chance coincidences, new features appear at recently dead sites more often on the early-M dwarfs than on G–K light curves degraded to the same sensitivity (Section 3.4). The Sun, forward-modeled as a Kepler target from its full sunspot-group record, fails the variability cut of these samples and yields too few trackable features in any four-year window for a survival fit (Section 3.6). In a model of a light-curve feature as a site of repeated flux emergence, the hazard of a site fed steadily enough settles to a constant after roughly one to two lifetimes of its member groups, even when those groups age (Section 3.8). No feeding configuration we tested, however, reproduces the flat hazard together with the observed lifetimes and depths, including the one in which the member groups themselves do not age.

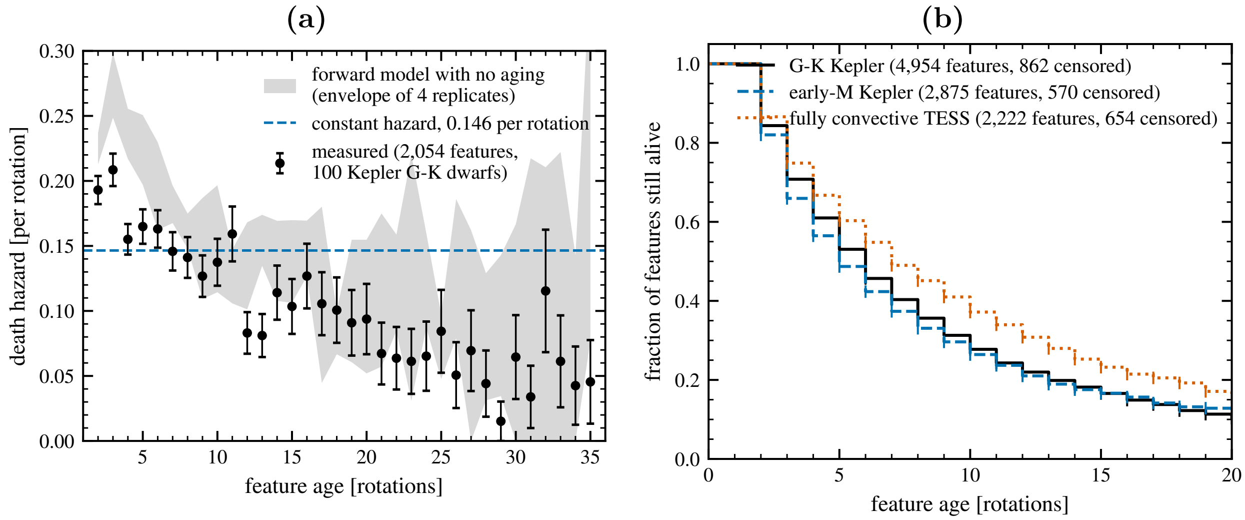

Figure 1: (a) Fraction of the tracked features alive at each age, in rotations, that die in the next rotation (the population hazard), for the 2,054 features on 100 Kepler G–K dwarfs (points with error bars). The gray band is the range of four simulated populations with no aging passed through the same detection and tracking, and the dashed line is the constant value fitted to the points, 0.146 per rotation. The measured and the simulated hazards decline together, so the decline reflects heterogeneity between features and the loss of shallow ones below threshold rather than aging; the band is drawn for its trend, not its level, which lies above the points. These points hold neither birth depth nor star fixed. The fit that does (Table 2) finds an age slope of 0.0056 per rotation, below the 95th percentile of the same fit on simulated populations without aging. This is the paper's main finding. (b) Kaplan–Meier survival of tracked features in the G–K, early-M, and fully convective samples, the fraction still alive at each age in rotations. Steps are deaths, each drawn at the first rotation of its death interval and counted before the censored histories that leave at the same age. Ticks are censored histories leaving the curve (862, 570, and 654, at data gaps, blends, or the end of the baseline). Median lifetimes are 6.0, 5.0, and 7.0 rotations (interval-censored estimates 6, 6, and 7; Section 3.2). On the fully convective sample, the tracking stretches long lifetimes (Appendix B), so that curve's upper tail is uncertain in both directions.

3.1 The death hazard as a function of age

At fixed birth depth and star-level frailty, a feature in its tenth rotation is at the same fitted risk of dying as one in its third, to within the scatter that simulated populations without aging show through the same analysis (Figure 1, Table 2). The ratio of observed deaths to those expected under the fitted no-aging model falls from about 1.4 in the first rotations after confirmation to below one beyond twenty rotations, in the data and in four simulated populations without aging alike. Tracked features thus die fastest just after confirmation whether or not spots age, and the fitted age slope measures the departure from this shared pattern.

On the G–K sample the fitted Gompertz slope is $\hat{B} = 0.0056$ per rotation and the AIC gain of the aging model is 1.17. Among 300 simulated G–K populations with no aging passed through the same detection, tracking, and fit, 57% give a smaller slope and 59% a smaller gain. Their 95th percentiles are 0.0137 and 12.4, and their 99th percentiles 0.0152 and 16.3 (Table 2). Restricting the

Table 2: Survival-fit results for the three samples. Beside each fitted slope $\hat{B}$ and AIC gain ΔAIC the table lists the 95th percentile of the same quantity over 300 simulated populations with no aging passed through the same detection, tracking, and fit, with its Monte Carlo standard error (Section 2.4). In both Kepler samples $\hat{B}$ and ΔAIC fall below those percentiles, so we detect no rise of the hazard with age. The fully convective values also fall below their percentiles, which we list in parentheses without using them as a bound because those simulations do not preserve feature identity (Appendix B). Injected aging of 0.05 per rotation or more on G–K, and of 0.12 or more on early M, is detected in at least 90% of simulated populations for every end-of-life profile (Section 2.4). Detection here means a positive slope with an AIC gain above the 95th percentile of the same-profile simulations without aging. The early-M figure carries the reservations of Section 3.4. Counts are the stars with at least ten tracked features (89 of the 100-star G–K core sample; 137 and 34 of the full early-M and fully convective samples), and medians are of completed lifetimes. In the recurrence column the parenthesis is the binomial standard error in percentage points, and the G–K and early-M nulls carry their standard deviation over 1,000 within-star permutations. A bootstrap over stars gives 0.98 and 1.26 points for the G–K and early-M rates. The G–K row at early-M sensitivity is the same 100 stars with noise added (Section 2.5), and the fully convective rate is listed beside its null but not claimed (Section 3.5). The days-versus-period slopes carry bootstrap 95% intervals or standard errors over stars.

Sample	Stars	Features	Deaths	$\hat{B}$	no-aging $\hat{B}$, 95th pct.	ΔAIC	no-aging ΔAIC, 95th pct.	Med. life [rot]
G–K dwarfs	89	1,988	1,662	$+0.0056$	0.0137 ± 0.0005	1.17	12.4 ± 1.1	5.0
Early-M dwarfs	137	2,332	1,943	-0.0073	0.0123 ± 0.0008	4.09	10.7 ± 1.0	4.0
Fully convective	34	2,197	1,550	-0.0019	(0.0290 ± 0.0011)	-1.59	(42.3 ± 1.9)	5.0 [3.0, 10.0]

Sample	days-vs-P slope	Recurrence vs occupancy null [%]
G–K dwarfs	0.890 $[0.617, 1.168]$	13.29 (0.75) / 13.91 ± 0.69
G–K at early-M sensitivity	...	19.58 (0.76) / 18.29 ± 0.62
Early-M dwarfs	0.769 $[0.675, 0.860]$	20.83 (0.76) / 16.33 ± 0.58
Fully convective	0.976 ± 0.109	40.64 (1.04) / 23.32

fit to the 81 core stars inside the 249-star selection (1,830 features, 1,526 deaths) gives $\hat{B} = 0.0061$ and a gain of 1.50. Injected aging of 0.05 per rotation or more would have been detected for every end-of-life profile, and 0.08 or more against the 99th percentiles (Section 2.4). With the three profiles combined, the measured slope lies inside the central 95% of the slopes fitted to simulated populations injected with B between -0.02, the most negative value we tried on this sample, and $+0.02$ per rotation. It lies outside that range for every injected value of 0.03 or more.

The 95% profile-likelihood intervals on $\hat{B}$ (a drop of 1.92 in log-likelihood) are -0.001 to $+0.012$ (G–K), -0.014 to -0.001 (early M), and -0.008 to $+0.004$ (fully convective). The early-M interval excludes zero on the negative side, so at fixed birth depth and star the fitted hazard declines slightly with age. All 300 simulated early-M populations with no aging return a larger slope through the same analysis, from -0.0067 to $+0.0173$, so the tracking, as simulated, does not produce this decline. The profile-likelihood interval and the comparison with simulations thus agree that the hazard does not rise with age, which is the alternative our test is built to detect. The AIC gain of the aging model, 4.09, lies below the no-aging 95th and 99th percentiles of 10.7 and 16.1. Populations injected with a slightly declining hazard, $B = -0.01$ to -0.03 per rotation, still return fitted slopes centered above zero (medians 0.003 to 0.007), above the measured slope like those of the populations without aging. At every injected value from -0.03 to solar strength the measured slope lies below the central 95% of the fitted ones. In this respect the early-M simulations, in which only about half of the fitted features begin at an injected spot (Section 2.4), do not reproduce the data. A refit at fixed current depth, reported at the end of this section, reverses the sign of this slope without closing its offset from the simulations.

The fitted frailty variance σ^2 and depth coefficient β_d of Equation 1 are 0.063 and -0.33 (G–K), 0.072 and -0.35 (early M), and 0.018 and -0.42 (fully convective). The last variance lies at the lower edge of the range that our numerical integration over the frailty covered. Widening that range puts the fully convective variance at 0.012 (95% interval 0.005–0.021) and moves that sample's slope and AIC gain to -0.0029 and -1.10. Forcing the variance to zero instead gives -0.0052 and $+1.07$, at a cost of 16.3 in twice the log-likelihood. The fully convective hazard thus shows no rise under any treatment of the frailty. On the G–K sample the Weibull-type form of Equation 1 fits better than the memoryless one by $\Delta\text{AIC} = 92$, but the 300 simulated G–K populations without aging give a median of 73 and a 95th percentile of 109 for the same comparison. We trace that preference chiefly to the rotation of the confirming sighting, which in the data and the simulations alike counts toward the time at risk but cannot contain a death (Section 2.3). The Weibull-type term thus describes the tracking rather than the spots. On the other two samples the simulations give larger values than the data, and we read only the Gompertz slope, calibrated in the same way, for aging.

The solar fit of the companion paper holds a group's current area fixed, whereas the fits above hold a feature's depth at birth fixed (Section 2.3). We therefore also refit the two Kepler samples with the feature's depth at each sighting as a covariate that changes from rotation to rotation, as the group's area does in the solar fit. On G–K this raises the slope from 0.0056 to 0.0121 per rotation (95% interval 0.006 to 0.018) and the AIC gain from 1.17 to 14.1. The same refit also raises the slopes of the 300 simulated populations without aging, by 0.0022 at their median and 0.0063 at their 97.5th percentile, against the observed rise of 0.0065. Their slopes then reach 0.0144 at the 95th percentile, above the observed 0.0121. The refit places the observed AIC gain at their 94th percentile ($p = 0.057$), within the Monte Carlo uncertainty of the 95th. At fixed current depth, then, the comparison neither detects aging at the 5% level nor excludes it as firmly as at fixed birth depth. Judged against the 95th percentile of those simulations with the three profiles combined, solar-strength aging is detected under this refit in all 90 simulated populations, and aging of $B = 0.05$ in 78 of 90. On early M the refit gives $+0.0019$ per rotation (-0.0040 to $+0.0076$) in place of the decline at fixed birth depth. The slopes of the simulated early-M populations without aging rise by as much, 0.0054 to 0.0140 over their central 95% against the observed 0.0092, so the sign of that decline is a property of the covariate. Under either covariate the measured early-M slope lies below all 300 of those populations, about 0.012 per rotation below their median, and that offset is what the early-M simulations leave unexplained (Section 3.4).

The flat hazard holds in each of the five temperature bins of the G–K sample, 3900 to 6000 K, where the median lifetime is 5.0 rotations in every bin and the median in days runs from 54.5 d in the coolest bin to 38.8 d in the hottest. In four of the five bins the fitted slope and AIC gain lie under the pooled sample's no-aging 95th percentiles of 0.0137 and 12.4. The 4400–4900 K bin gives $\hat{B} = 0.0235$ with $\Delta\text{AIC} = 7.5$, a slope above the 0.0137 percentile, so we tested it against 99 simulated data sets with no aging built on its own stars. These simulations give slopes from

−0.0115 to +0.0354 and ΔAIC up to 18.4, and 8 of the 99 reach the observed slope and 11 of the 99 the observed ΔAIC, so the bin is consistent with no aging.

3.2 Median lifetimes and the tracking ceiling

The median completed lifetimes are 5.0, 4.0, and 5.0 rotations in the three samples. The Kaplan–Meier estimator, which keeps each censored history alive for as long as we watched it and places each death at the start of its interval, gives medians of 6.0, 5.0, and 7.0 rotations on the full samples (Table 2, Figure 1b). The nonparametric maximum-likelihood estimator for interval-censored lifetimes, which spreads each death over the two or more rotations of its interval, gives 6, 6, and 7. Its survival curves differ from the Kaplan–Meier ones by at most 0.03 beyond age 5. In 1,996 of 2,000 bootstrap resamples the G–K Kaplan–Meier median is 6.0 rotations, and across the resamples the early-M and fully convective medians range from 5.0 to 6.0 and from 7.0 to 8.0. The median lifetime therefore spans 4–7 rotations across the two estimators and the three samples, with values above ∼6 rotations compressed by the tracking ceiling.

A lifetime can be fixed in days or in rotations. An injection test on quiet Kepler light curves tells the two apart for lifetimes inside the tracking window, those below the ceiling of about six to seven rotations measured later in this section. For features injected with lifetimes fixed in days between 15 and 60 d, the recovered lifetime in days rises only slowly with the period (slope $d\log(\text{days})/d\log P = 0.153$ over the injection grid above the visibility limit, Appendix A). The slope is 0.42 when births are injected at a fixed rate per rotation rather than per day. For features injected with lifetimes fixed in rotations, the recovered lifetime in days rises with the period at slope 1.000, with a median of 4.0 rotations at every period. The 98 stars of the G–K core sample with at least five tracked features give an observed slope of 0.890 with bootstrap 95% interval $[0.617, 1.168]$ (Figure 2). That slope lies 5.2 standard errors from the fixed-day value of 0.153, or 3.3 from the 0.42 for births fixed per rotation, and 0.8 from the fixed-rotation value of 1.000. Simulated populations on the time sampling and noise of the 100 core stars, with birth rates calibrated to their crowding, give the same separation inside the tracking window. Lifetimes fixed at 25 or 40 d return slopes of 0.203 and 0.254, more than four standard errors below the observed one, with median lifetimes of 23 and 33 d against the observed 47 d. Lifetimes fixed at 5, 8, or 12 rotations return 0.969–1.078. For true lifetimes inside that window the lifetime of a tracked feature is therefore set in rotations, and the analysis does not impose this unit.

A lifetime that outlasted the tracking ceiling at every period would, however, be returned near the ceiling, in rotations. Injected populations with lifetimes fixed at 90 to 300 d are recovered at medians of 4 to 6.5 rotations with slopes of 0.719 to 1.163, inside the observed interval, and neither their site-recurrence rates nor their upper quartiles set them apart. The slope therefore excludes lifetimes fixed at 25 to 40 d by more than four standard errors and disfavors 60 d at 2.8, but does not exclude a population of much longer-lived features seen through the ceiling. Period and temperature correlate in this sample (Spearman rank correlation −0.35, $p = 4.7 \times 10^{-4}$), so a day-valued lifetime that varied with temperature could shift the slope, but it would have to mimic a lifetime proportional to period across the observed range.

The quiet-star injections of Appendix A also measure the window of lifetimes that the analysis can recover. Because the tracking returns a true lifetime beyond the upper edge of that window at a value inside it, the medians near that edge are lower limits. We recovered injected lifetimes of 8 rotations at 5.75–7.0 rotations, and an injected lifetime of 12 rotations at a median of 5.5, with the individual simulations ranging from 4.0 to 7.5, so the analysis has a tracking ceiling of

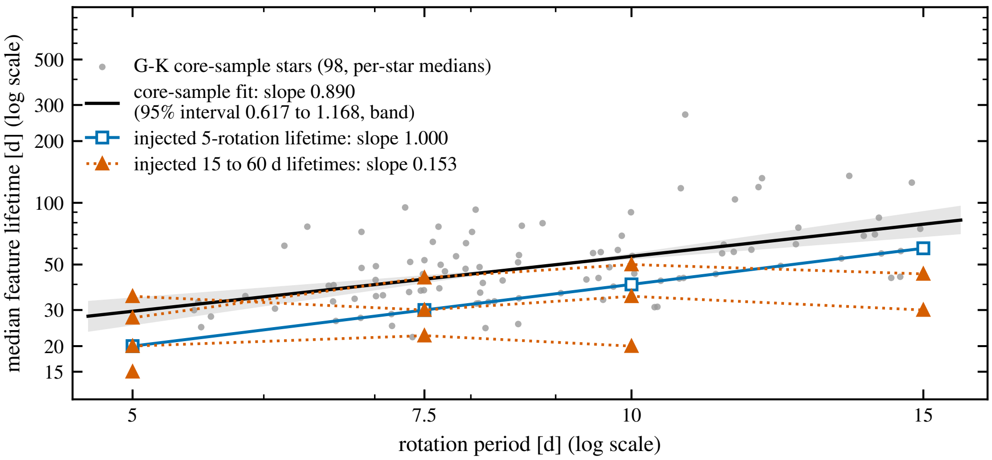

Figure 2: Median lifetime in days against rotation period for the 98 stars of the G–K core sample with at least five tracked features (gray dots, with their fitted power law as the black line and its bootstrap 95% band shaded), for features injected into quiet Kepler light curves with a fixed five-rotation lifetime (blue squares), and for features injected with lifetimes fixed at 15 to 60 d (orange triangles). The real stars (gray dots, slope 0.890 with interval 0.617 to 1.168) follow the fixed-rotation injections (blue squares, slope 1.000) and not the fixed-day injections (orange triangles, slope 0.153). The fixed-day features here live 15 to 60 d and are born at a fixed rate per day. A feature that the tracking can follow therefore has its lifetime set in rotations (Section 3.2).

about 6–7 rotations. The ceiling comes from track breakage, in which accumulated phase drift and sub-threshold profile tails produce false deaths under the two-miss rule and the fragments re-enter as new births at the same site. Inside the window the ratio of recovered to injected lifetime in days runs from 0.75 to 1.00, and from 0.75 to 0.88 for injected lifetimes of 4–6 rotations, where the measured completed medians lie. For the G–K sample, and for true lifetimes inside this window, the day-valued medians are therefore 12–25% low, and for true lifetimes beyond the ceiling they are lower limits only. On the fully convective sample, where injected eight-rotation features are recovered one rotation too long in the median (Appendix B), we quote no correction.

3.3 Rotation period versus Rossby number as the lifetime clock

The lifetime in days rises with the rotation period, as a power law in the period alone, $L = 10^{0.868}\,P^{0.828}$ days, fitted on the 438 stars of both Kepler samples that have at least three feature deaths and so enter the per-star fit, with a weighted rms of 0.1443 dex (Figure 3b). The exponent has a bootstrap 95% interval of $[0.767, 0.887]$ over 10,000 resamples of the stars.

If the lifetime were set by the Rossby number, the rotation period divided by a convective turnover time (Noyes et al., 1984; Wright et al., 2011), rather than by the period itself, replacing the period by that ratio should tighten the fit (Figure 3a). We tested five published turnover scales, the empirical scalings of Cranmer and Saar (2011), Wright et al. (2011), and Wright et al. (2018), and both the empirical and the MESA-model turnover tables of Gossage et al. (2025). Each of the five substitutions loosens the per-star fit (negative Δrms in Table 3), and the Rossby form tightens the fit in none of 10,000 bootstrap resamples at any scale.

We also let the turnover time τ_c enter with its own exponent, fitting $\log L = c + \alpha \log P + \gamma \log \tau_c$

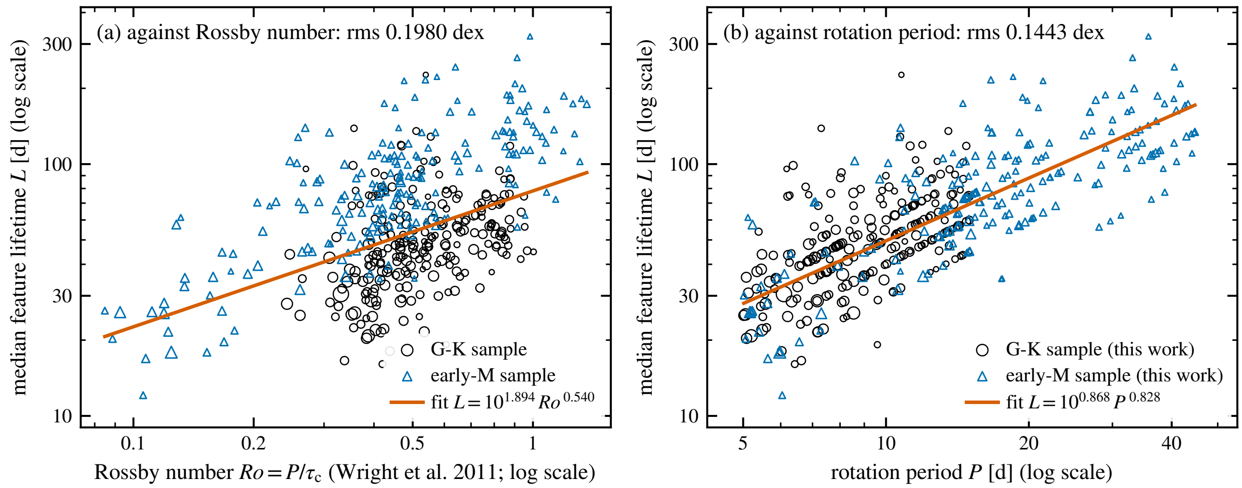

Figure 3: Median lifetime of tracked features in days for the 438 Kepler stars of the G–K sample (circles) and the early-M sample (triangles), against the Rossby number P/τ_c with the turnover time τ_c of Wright et al. (2011) in (a) and against the rotation period P in (b), each panel with its own fitted power law (line). Symbol area scales with the number of deaths on the star, which is the star's weight in the fit, and the per-star medians carry no other recorded uncertainty. The rotation period alone fits the lifetimes more tightly than the Rossby number does, with a scatter about the line of 0.1443 dex in (b) against 0.1980 dex in (a); the fit in (b) is $L = 10^{0.868}\,P^{0.828}$ d.

Table 3: The rotation period gives the smallest scatter of the candidate clocks, in the per-star fit and across the six subsamples. For each clock the table gives the weighted rms of the per-star lifetime fit in that unit and the change in rms when the turnover form replaces the rotation-alone law, a negative change meaning that the substitution loosens the fit. The last two columns give the number of bootstrap resamples of the stars, of 10,000, in which the substitution tightened the fit, and the rms log-scatter of the six subsample median lifetimes in that unit.

Clock	Source	Fit rms [dex]	Δrms	Resamples	Scatter [dex]
Rotation period P	**this work**	**0.1443**	...	...	**0.0396**
Raw days	...	...	...	...	0.0936
Ro, CS11	Cranmer and Saar (2011)	0.2147	−0.0704	0/10,000	0.14
Ro, W11	Wright et al. (2011)	0.1980	−0.0537	0/10,000	0.0744
Ro, W18	Wright et al. (2018)	0.2123	−0.0680	0/10,000	0.1183
Ro, Gossage 2025 empirical	Gossage et al. (2025)	0.2256	−0.0813	0/10,000	0.2131
Ro, Gossage 2025 MESA	Gossage et al. (2025)	0.2224	−0.0781	0/10,000	0.1662

with c, α, and γ free. Across the five scales γ lies between -0.074 and -0.021 and α between 0.839 and 0.859, each γ within two bootstrap standard deviations (0.024 to 0.047) of zero. A lifetime set by the Rossby number would require $\gamma = -\alpha$ and one counted in turnover times $\gamma = +\alpha$. The data allow a turnover dependence of at most 18% of the period dependence in magnitude ($|\gamma/\alpha| \leq 0.18$ at the 97.5th percentile), negative in sign. Adding the turnover term improves the prediction of held-out stars by at most 0.2% of the scatter for any scale. It worsens the pooled prediction of the six held-out subsamples, though not of every subsample singly, and the prediction of either spectral class from the other. Adding each star's variability amplitude and brightness as covariates leaves γ inside its interval. Within the early-M sample alone, however, γ is negative at more than three standard deviations for every scale and remains so with those covariates added, while within G–K it is consistent with zero with the opposite sign. This term therefore follows temperature within the early-M sample, and these data do not decide whether its origin is physical or lies in the detection differences along that sample. Across the six subsamples (the five G–K temperature bins and the early-M sample) the rms scatter of the median lifetimes is also smallest in the rotation unit (Table 3). The Gossage et al. (2025) table has a spike at $0.30\,M_{\odot}$, near the fully convective boundary, where the empirical turnover time is 239.77 ± 49.66 days against 135.36 ± 10.04 days in the neighboring $0.38\,M_{\odot}$ bin, and their theoretical values are 451 against 84 days. We nevertheless use the turnover tables as published, including the spike, so the preference for the rotation period over the Rossby number holds only for the five scales tested.

3.4 Comparison of the G–K and early-M samples

On the early-M sample a new feature appears at the phase of a recently dead one at a rate of 20.83%, against $16.33 \pm 0.58\%$ in 1,000 permutations of feature positions within each star (the occupancy null of Section 2.5), none of which reaches the observed rate. An excess over this null does not by itself imply a memory of sites (Section 2.5). The G–K core sample shows no such excess; the rate there, 13.29%, lies inside its own permutation distribution ($13.91 \pm 0.69\%$; $z = -0.89$, $p = 0.809$). However, most of the difference between the raw early-M and G–K recurrence rates comes from the unequal sensitivity of the two samples (Section 2.5).

Degrading the G–K core sample to early-M sensitivity raises its rate to 19.6% and its occupancy null to 18.3%, because the added noise breaks each feature into more and shorter tracks (2,743 tracked features against 2,054 on the same light curves at full sensitivity). Only 22 of 1,000 permutations reach the remaining excess of 1.3 ± 0.8 percentage points. Since the same stars show no excess at full sensitivity, fragmentation alone produces an excess over this null (Table 2). The survival fit on the degraded G–K light curves still gives a flat hazard, $\hat{B} = 0.004$ per rotation with an AIC gain of 0.2, below the no-aging 95th percentiles of the undegraded sample in Table 2. The median lifetime in rotations is also the same before and after the degradation. At matched sensitivity the early-M excess over its own null, 4.5 ± 0.9 points, exceeds the degraded G–K excess by 3.2 ± 1.2 points, or 2.7 standard errors with a bootstrap over stars. Adding the permutation scatter of both nulls lowers this to 1.9 standard errors. Half of the early-M excess comes from ten of the 230 stars. Simulated populations with no memory of sites, passed through the same tracking, also return excesses over this null that grow with the density of tracks, because on a crowded star a death frees room in rotational phase for new detections, an effect the permutation does not reproduce. The early-M excess by itself therefore does not measure re-emergence at dead sites, and only its difference from the matched G–K sample is evidence of a class difference.

The early-M per-star medians give a days-versus-period slope of 0.769 (bootstrap 95% interval $[0.675, 0.860]$; Table 2). In simulated early-M populations on these stars' own time sampling, noise, and calibrated crowding, lifetimes fixed at 5 to 12 rotations return slopes of 0.931–1.036, and lifetimes fixed at 40 to 90 d return 0.529–0.597. Each lies three or more standard errors from the observed value. A lifetime fixed at 25 d fails instead on its median, 33 d against the observed 83.5 d. One fixed near 150 d, beyond the tracking ceiling at most of these periods, returns a slope of 0.808 and a median in days close to the observed one. The early-M lifetimes thus rise with the period less steeply than a pure count of rotations does in that sample's simulations, and the slope alone does not exclude a population of long-lived features seen through the ceiling (Section 3.2).

As on G–K (Section 2.4), we measured by injection how much intrinsic aging the flat early-M hazard excludes, with the same three end-of-life profiles. The injected aging slopes lie on a grid from -0.03 to 3.336 per rotation, whose upper end is solar-strength aging on this sample's rotation clock, the solar $+0.184$ per day multiplied by the sample's median rotation period. At each slope and profile we built 30 populations matched in size to the fitted sample. We count aging as detected by the rule of Section 2.4. Aging of 0.12 per rotation or more is detected in at least 27 of 30 populations for every profile, and of 0.18 or more in all 30. In these simulations, then, aging of 0.12 per rotation or more would have been detected for every end-of-life profile, and 0.18 or more against the 99th percentile instead. Solar-strength aging is detected in all 30 populations of each profile, although the recovered slope saturates near 0.03 per rotation and so does not measure its strength. The corresponding G–K bound is 0.05 per rotation for every profile, with solar strength detected in every population (Section 2.4). These early-M bounds rest on a noise model that we could check only on G–K hosts (Appendix B). They also rest on simulations that reproduce neither the measured early-M slope (Section 3.1) nor the depths of real features in the rotations before their last detection (Section 2.4). The early-M baseline is also shorter, 96 observed rotations per star on average against 172 on G–K. For these reasons 0.12 per rotation is the sensitivity of the early-M simulations, and as a bound on the stars it is less secure than the G–K bound.

3.5 Across the fully convective boundary

Past the fully convective boundary the slope of the per-star median lifetime in days against rotation period is 0.976 ± 0.109 (Figure 4a). This slope lies 0.2 standard errors from the value of 1 expected for a lifetime fixed in rotations, but on this sample that comparison does not identify the clock. Populations injected into simulated light curves on these stars' own time sampling, with lifetimes fixed at 5 to 80 d or from 3 to 12 rotations, all return slopes of 0.827–1.112 and median tracked lifetimes of 4–5 rotations. On these crowded light curves the tracking, not the injected lifetime, sets the distribution of tracked lifetimes. A feature that outlives this sample's own ceiling of about five rotations is returned near it, and shorter-lived ones are lengthened by the capture of neighboring features. The fixed-day reference of Section 3.2, measured on Kepler light curves at periods of 5–15 d, therefore does not transfer to this sample, and the slope establishes only that the tracked lifetimes count rotations. The median lifetime is 5.0 rotations, equal to the G–K median of Section 3.2, with interquartile range [3.0, 10.0] (Table 2). We do not interpret the upper quartile, which lies above the tracking ceiling on light curves where injected features come back longer than injected (Appendix B).

The injected control features also overlapped these stars' own features too often for the tracking to keep their identities. Simulated populations with no aging on these stars' time sampling and noise return positive slopes, median 0.020 per rotation against the -0.0019 measured, and AIC gains with a 95th percentile of 42.3, far above the measured -1.59 (Table 2). Injected aging of solar strength, 0.594 per rotation at the median period, clears their 95th percentile in only 14 to 27 of 30 populations, depending on the end-of-life profile (Appendix B). These simulations cannot calibrate aging here, so the flat hazard on this sample is a consistency check and not a bound. In a separate injection run we recovered the injected site recurrences at a mean net rate of 0.4295 (Section 2.5), below the 0.50 we required, so this sample's high raw recurrence rate (Table 2) does not establish an excess (Appendix B). The median tracked lifetime in rotations and the days-versus-period slope agree with the Kepler samples across the boundary, but this sample does not determine whether the death law and the physical clock continue across it.

3.6 The Sun as a Kepler target

The Sun would not enter the samples of this paper, since its rotational variability lies below the selection cut of Section 2.1. Forward-modeled as a Kepler target, it also yields too few trackable features in any four-year window for a survival fit (Figure 4b). We forward-modeled into Kepler long-cadence photometry every recorded disk passage of a sunspot group in the daily record from which the registry of Section 2.1 is drawn, 42,580 passages of 42,561 groups. Geometry and spot contrast are the only physics assumptions, and the model carries the measured bright-star noise of our own sample (median 156 ppm per cadence). The birth-observed registry of Section 2.1 is the subset of 25,883 passages that begin far enough from the east limb for the birth to be seen, and it holds 19% of the on-disk spot area in the 13 solar-maximum windows analyzed here. We then passed 13 four-year solar-maximum windows through the same detection and tracking rules as the stars. In these 52 years of solar-maximum observing the modeled Sun yields 87 confirmed features and 82 deaths, between 1 and 13 per four-year window, or 1.7 per year of solar maximum. The birth-observed subset alone yields one feature. At that rate a survival fit, which needs at least 50 features and 20 deaths over three or more windows, takes about thirty years of solar maximum, and no single Kepler-length window supplies it. The variability cut excludes the Sun even though its dips are often deep. Its modeled spot deficit exceeds the 1,000-ppm depth threshold on 3,591 of the 18,980 days in these windows, with a 99th percentile over the whole record of 2,144 ppm and a maximum of 4,656 ppm in January 1959. These days give 438 dip detections and the 87 confirmed features above.

Irradiance instruments record the passages of large spot groups as drops in total solar irradiance roughly proportional to spot area (Toriumi et al., 2020), and the record short-term drop, 0.34% under the large groups of late October 2003 (Kopp, 2016), tests the model's amplitude scale. Our forward model, with the recorded areas at the published bolometric spot contrast of 0.32 ($K = 1$ in Figure 4b), gives 3,312 and 3,389 ppm on 2003 October 30 and 31 against the 3,400 ppm observed at that dip. The birth-observed registry alone gives 1,495 ppm, because the two largest groups of that passage, NOAA 10484 and 10486, were first recorded too close to the east limb to count as observed from birth. Regressed on the modeled deficit over the 4,834 days of 1978–2020 with at least 300 ppm modeled, the observed daily total-irradiance deficit has a slope of 0.71 ± 0.01, below unity as expected since the model omits facular brightening. We therefore adopt $K = 1$ for the Sun. As a check of the forward model, the observed irradiance itself, passed through the same detection and tracking in the three windows it covers completely, gives 6, 3, and 1 confirmed features where the model gives 9, 1, and 2.

The count is sensitive to the modeled amplitude, 51 features at $K = 0.75$ and 133 at $K = 1.25$. No single four-year window holds more than 13 features at $K = 1$, or more than 32 even at $K = 5$. We do not fit the 87 features for aging. Simulated solar registries whose groups die without aging, built on the birth-observed registry at five times its modeled amplitude and passed through the same detection and tracking, return rising fitted hazards, as the fully convective simulations do (Section 3.5).

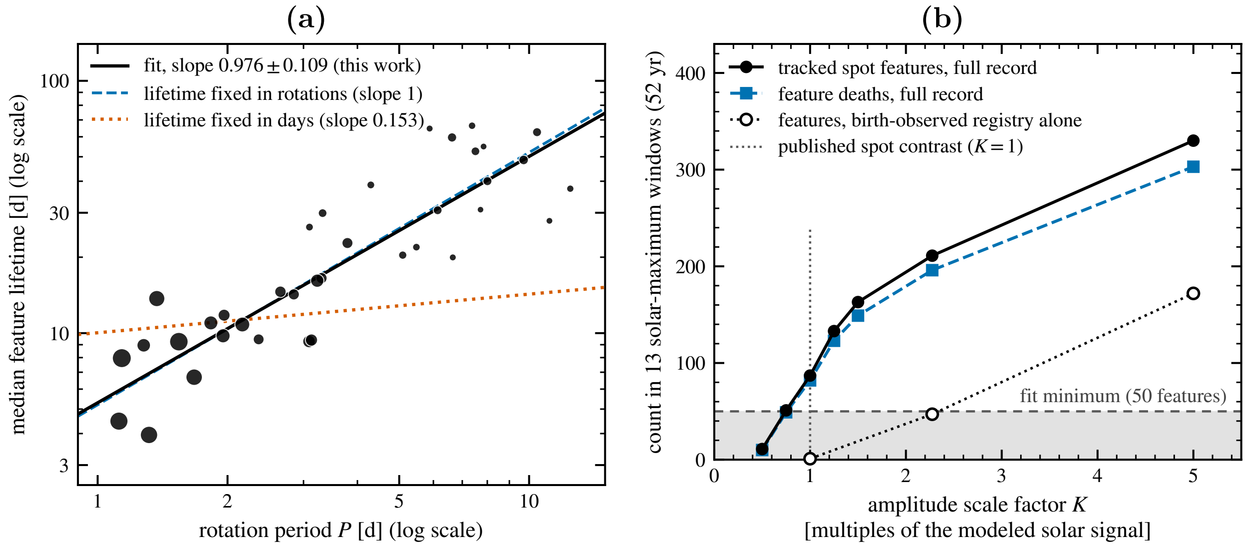

Figure 4: (a) Median lifetime of tracked features at death, in days, against rotation period for the 37 TESS dwarfs past the fully convective boundary (periods 1.1 to 12.5 d), on logarithmic axes, with symbol area scaling with the number of deaths on the star. The solid line is a power law fitted to these per-star medians by least squares in the logarithms, weighted by the number of deaths, with slope 0.976 ± 0.109 (bootstrap 95% interval 0.764 to 1.191). The dashed line through the weighted centroid has the slope of 1 expected for a lifetime fixed in rotations. The dotted line has the slope 0.153 of the fixed-day injections of Section 3.2, a Kepler reference that does not apply at these periods (Section 3.5). The tracked lifetime thus scales with the rotation period past the boundary, though on this sample that scaling does not by itself identify the physical clock (Section 3.5). (b) Confirmed tracked features (black circles) and feature deaths (blue squares) recovered from the forward-modeled full sunspot-group record in 13 four-year solar-maximum windows, 52 years in all, against the factor K by which the modeled solar signal is scaled. $K = 1$ is the published spot contrast, which reproduces the 2003 October irradiance dip, and open circles show the birth-observed registry alone. The gray region lies below the fit minimum (50 features, 20 deaths, 3 windows), which the full record clears at $K \geq 0.75$ and the birth-observed registry only at $K = 5$. The Sun as a Kepler target thus yields fewer than two trackable features per year of solar maximum, too few in any single four-year window for a survival fit.

3.7 Comparison with HARPS-N solar radial velocities

The Sun would not enter the photometric samples of Section 3.6, but its active regions also modulate its disk-integrated radial velocity. If those regions persist for the feature lifetimes measured here, carried to the Sun, the autocorrelation of the velocity at a lag of two rotations is a predictable fraction of its value at one rotation. On the decade of HARPS-N solar velocities reported by Dumusque et al. (2026), reduced to 2,069 daily medians in four seasons, that fraction, the whole-rotation autocorrelation ratio $T_2 = \rho(2P)/\rho(P)$, is 0.68 with a 95% interval of $[0.36, 0.93]$. We use the ratio because the short-memory signals in the velocities (granulation, supergranulation, and the day-to-day zero point) decorrelate at lags far below one rotation and lower each whole-rotation correlation by a common factor, which cancels in the ratio. In every configuration we computed (Appendix C) the interval lies entirely above the reference interval $[-1.63, -0.08]$ of the quasi-periodic kernel of Klein et al. (2024). We took that kernel season by season, with the squared-exponential envelope (decay times 18 to 22 d), rotation period, and harmonic complexity that they fitted to the total observed velocity. We simulated it on the observation dates of the series analyzed here and passed it through the same detrending. The observed interval overlaps both intervals predicted from the stellar lifetime law, $[0.32, 0.44]$ for lifetimes carried to the Sun in days and $[0.60, 0.70]$ for lifetimes scaled to its rotation period, so the test cannot tell the two forms apart. The Sun lies outside the measured range of the law on both axes, with a 27-d rotation period beyond the G–K sample's 5 to 15 d (Table 1) and an activity level below the variability cut that sample had to clear, so the comparison tests an extrapolation. The overlap is consistent with active regions that modulate the solar radial velocity, mostly through faculae and plage (Haywood et al., 2016), and persist on the timescale of the tracked features. With an interval this wide, however, the test would identify either form of the law in only 0.35 to 0.41 of simulated cases (Appendix C), so it is a consistency check and not a measurement of that timescale.

3.8 Relation to the aging of individual sunspot groups

We interpret a tracked feature in a light curve as a site fed by ongoing emergence, the stellar counterpart of a sunspot nest (Castenmiller et al., 1986), which dies when its population of member spot groups first reaches zero. In the model below, the death hazard of such a site under steady feeding tends to a constant even when its groups age. At feeding rates up to 0.15 groups per day it first rises, and settles only after a transient of one to two member-group lifetimes. Whether the constant is reached within the observed feature lifetimes depends on the feeding rate and on the groups' lifetime law. On the Sun a group's log death hazard rises by +0.184 per day at fixed current area (Schwartz and Garraffo, 2026). On the G–K stars the flat hazard excludes aging at 0.05 per rotation and above for every end-of-life profile tested by injection (Section 2.4). On the G–K rotation clock the solar rate is 0.184 per day times the median rotation period of the 249 selected G–K stars, 9.59 d, or 1.765 per rotation, about 35 times that bound. The solar rate refers to a resolved sunspot group in a 150-year registry, and the stellar bound to an unresolved photometric feature that can contain many groups. The two also answer different conditional questions, since the solar fit holds the group's current area fixed and the stellar fits hold the feature's depth at birth fixed (Section 2.3). With the stellar fits conditioned on current depth instead, the G–K slope is +0.012 per rotation, at the 89th percentile of the same fits on simulated populations without aging. The AIC gain of the aging model is at their 94th percentile ($p = 0.057$), so that comparison, too, detects no aging at the 5% level, though less firmly (Section 3.1). Namekata et al. (2020) find many transit-mapped spots on stars whose light curves show only two minima per rotation, and Basri et al. (2022) read their own measured lifetimes as referring more to starspot groups than to individual spots.

In the model we analyze, time runs in days. A feature is born with $n_0 \geq 1$ members; while feeding is on, each day $t \geq 1$ brings a Poisson number of new members with mean f; each member lives for a lifetime ℓ drawn independently from a law $p(\ell)$ on $\{1, \ldots, L\}$, which may itself have a rising hazard; and the feature dies on the first day its member population $N(t)$ is empty,

$$T = \min\{\, t \geq 1 : N(t) = 0 \,\}, \qquad H(t) = \Pr(T = t \mid T > t - 1). \tag{4}$$

Under sustained, time-homogeneous feeding, with $f > 0$ and $p(L) > 0$ for a finite longest lifetime L, the feature hazard converges geometrically to a constant,

$$H(t) \to H_\infty = 1 - \rho \le e^{-f}, \tag{5}$$

where ρ is the largest eigenvalue of the matrix Q of one-day transition probabilities of the longest remaining member lifetime, restricted to the living states $\{1, \ldots, L\}$. The existence of a constant limit and the bound e^{-f} hold for every member law in this class, whether the members' own hazard rises, is flat, or falls. Both the value of the limit and the rate of approach depend on f and on $p(\ell)$. The limit is $H_\infty = \pi_1 e^{-f}$, where π_1 is the long-run probability that the longest-lived member present is in its last day, and the rate of approach is set by the ratio of the second eigenvalue of Q to ρ. Members that last exactly two days, for example, bridge an arrival-free day that members lasting one day cannot, and give a smaller H_∞ at the same f. For member groups obeying the solar death law (mean lifetime 34 d) at feeding rates of 0.02 to 0.15 groups per day, the approach has an e-folding time of 6 to 11 d. The hazard comes within 10% of H_∞ only after 33 to 55 d and rises until then. That is about four to seven rotations at the core sample's median period of 8.3 d, so over the feature ages observed here such a site is still in the transient unless its members are short-lived compared with the feature. When feeding stops at a time S, the feature outlives the feeding and dies within L days after it stops, except on an event of probability at most $\mathbb{E}[S]\, e^{-f}$. A site fed heavily enough that this probability is small therefore ends when its feeding does, to within the lifetimes of its last members, so that a memoryless feeding process gives a nearly memoryless feature. These results hold only for the model class tested. In that class the 44-day and 80-day configurations of Figure 5, whose feeding durations are exponentially distributed, are nearly degenerate in exact hazard slope, and they separate, 0.058 against 0.026 per day, only when the durations are fixed (Appendix D). Simulated light curves of the two fixed-duration configurations, passed through our analysis, separate in the same order, with median slopes of 0.102 and 0.070 per rotation.

Aggregation alone does not reproduce the flat stellar hazard from solar spot groups (Figure 5). We area-scaled complexes of spot groups obeying the measured solar death law until the forward model reproduced the G–K sample's dip depths, durations, and event rates, then passed them through the same analysis as the stars. The fits to these simulated complexes give median slopes of 0.049 to 0.164 per rotation across the feeding configurations, about 9 to 30 times the measured stellar value. The exact model also lets us feed solar-law groups faster or make them smaller and more numerous, down to 1/32 of the calibrated area. Carried through the measured attenuation of the tracking, the slope falls to the level of the stellar fits only where the features live nine or more rotations on average or are several times too shallow (Appendix D). Most of those configurations are both. Within this class, therefore, no feeding schedule of solar-law groups gives the flat hazard together with the observed lifetimes and depths. Member groups whose own death law is memoryless do not give the flat hazard either, in the one configuration of this kind that we tested. We built complexes of such groups with the solar mean lifetime of 34 d, fed as in the 44-day configuration of Figure 5 and rescaled to the same dip depths, durations, and event rates. Over four realizations they return a median slope of 0.024 per rotation and a median AIC gain of 36.5, both above the largest values among the 300 simulated G–K populations without aging (0.020 and 29.6; Section 3.1). Fed at that rate, such a site does not meet the heavy-feeding condition above. It is still in the transient while it is fed and then thins to its last members, so its hazard rises through our analysis whether or not those members age.

On the Sun, where nests are directly observable, we tested whether the nests themselves age. For nests as we identify them in the solar registry, the death law is memoryless (ΔAIC = 5.0, fitted

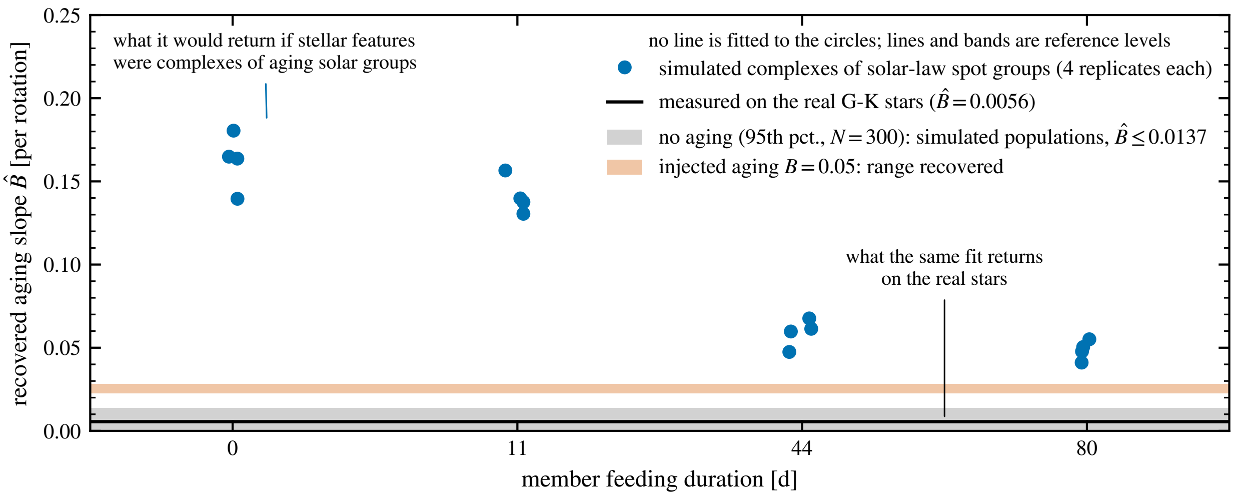

Figure 5: Recovered Gompertz aging slope $\hat{B}$ for simulated complexes whose member spot groups follow the measured solar death law, area scaled to the G–K sample and passed through the same analysis as the stars (blue circles, four replicates per configuration), against the duration over which new groups join each complex (0, 11, 44, and 80 d). No line is fitted to the circles, and the black line and the two bands are reference levels. The black line is the slope the same fit returns on the real G–K stars ($\hat{B} = 0.0056$ per rotation). The gray band is the range it returns on simulated populations without aging, up to their 95th percentile of 0.0137 (Table 2), and the orange band the range it recovers on four simulated populations injected with $B = 0.05$. The 44 d case reproduces the real sample's dip depths, durations, event counts, and death fraction. The circles lie far above all three levels, so stellar features assembled from aging solar groups would have shown aging in our fits; summing aging groups at these feeding rates does not produce the flat stellar hazard.

slope +0.001 per rotation). Here a nest is at least three groups whose births, in longitude corrected for differential rotation, fall within 7.5° of the running nest position and within 3.5° in latitude, each within three rotations of the previous member. We built the nests independently with two linking procedures that must agree, one adding each new group to the nearest running nest and one linking every pair of groups within those radii, and repeated the test with longitude radii of 5° to 15°. This nest test has power only against strong aging. The same analysis recovers an injected strong-aging law (site hazard e-folding over 1.5 rotations) in 7 of 8 and 6 of 8 simulated registries under the two procedures, but it cannot separate weaker aging laws from a memoryless one. On the Sun, then, individual spot groups age while nests do not, and the features tracked in stellar light curves behave like the nests. The solar nest statistics of Norton et al. (2026) and Zhao et al. (2026) are consistent with this identification, with nest lifetimes of 3.3 to 4.0 Carrington rotations, comparable to the median completed lifetimes of 4–5 rotations measured here, and 6 to 18% of emergence non-randomly nested.

4 Conclusions and discussion

4.1 Constraints on models

In these samples the tracked lifetime of light-curve features follows the rotation period and not the Rossby number built from any of the five tested turnover scales. Converting rotation to Rossby number through those scales (Cranmer and Saar, 2011; Wright et al., 2011, 2018; Gossage et al., 2025), taking the tables as published, tightens the lifetime fit in none of 10,000 bootstrap resamples (Section 3.3). Once the period is given, a free dependence on the convective turnover time is consistent with zero and at most 18% of the period dependence, negative in sign. The turnover time that organizes coronal and chromospheric activity is therefore not the clock of these features, though within the early-M sample alone a negative dependence on it appears whose origin these data do not settle. No sample shows aging. Injected aging of 0.05 per rotation on G–K, and, less securely, of 0.12 on early M (Section 3.4), would have been detected for every end-of-life profile tested, while the fully convective sample gives no bound. With the stellar fits conditioned on current depth, as the solar fit is on current area, the G–K comparison neither detects aging at the 5% level nor excludes it as firmly (Section 3.1). The tracked lifetimes rise with the rotation period from G dwarfs through early M and past the fully convective boundary (Sections 3.4 and 3.5), across the mass at which the tachocline disappears (Wright and Drake, 2016). Nothing in the fully convective sample calls for a mechanism tied to the tachocline. One measured difference between the spectral classes is the rate at which new features appear at recently dead sites. On the early-M dwarfs that rate exceeds its chance expectation by 3.2 ± 1.2 percentage points more than on G–K light curves degraded to the same sensitivity (Section 3.4). Half of the early-M excess sits on ten of the 230 stars. Because track fragmentation and crowding also produce such excesses on simulated stars with no memory of sites, we do not attribute the early-M excess to re-emergence at dead sites. A widely used light-curve forward model treats spot lifetime and nesting degree as interchangeable parameters and leaves the lifetime unconstrained (Nèmec et al., 2023; Sowmya et al., 2022). The death law measured here fixes the first of those parameters.

4.2 Discussion

Two explanations of the flat stellar hazard remain, and unresolved photometry cannot decide between them, but in the configurations of the fed-site model that we tested (Section 3.8) neither yields a flat hazard together with the observed lifetimes and depths. Either new spot groups feed a stellar feature faster than area-scaled solar spot groups do, so that supply dominates the turnover of stellar features, or the solar death law does not extrapolate to spots far larger than solar. The first explanation needs member groups that are short-lived compared with the feature as well as numerous. In the model of Section 3.8, groups that obey the solar death law hide their aging only when fed fast enough. At every group size down to 1/32 of the area-scaled calibration, such feeding makes the features live nine or more rotations on average, against observed medians of 5 to 6, or leaves them several times shallower than observed (Appendix D). The second explanation also fails in the one fed configuration we tested. Member groups with a memoryless death law and the solar mean lifetime, fed for 44 d on average as in Figure 5, still give a rising hazard through our analysis (Section 3.8). It would hold if each feature were a single structure whose own death is memoryless, the limiting case of the model with one member and no feeding. Resolved spot identities would show whether a stellar feature is one such structure or a complex of shorter-lived groups fed in a way we did not test. A Doppler-imaging time series of one heavily spotted dwarf, sampled every rotation or better across tens of rotations, would provide the life histories of resolved spots on a star other than the Sun and settle that question.

Ensemble measurements from autocorrelation and Fourier analyses (Giles et al., 2017; Basri et al., 2022; Degott et al., 2025) report lifetimes in days that are flat with rotation period or rise more slowly than it. But the tracked-spot measurements of Hall and Henry (1994), Namekata et al. (2019), and Tokuno et al. (2025) give lifetimes that rise with the period, as does the power law in rotation period fitted here.

The measured medians, 4–5 rotations for completed features and 5–7 by Kaplan–Meier, lie inside the range that Basri et al. (2022) calibrated in rotation units for the McQuillan et al. (2014) sample, with most stars above two rotations and half below eight. The lifetimes of the 56 tracked Kepler spots of Namekata et al. (2019), divided by each star's rotation period, have a median of 10.1 rotations (quartiles 6.3 to 16.9), about twice the medians measured here. The selection biases of the two samples run in opposite directions, since their tracker misses spots that live less than about two rotations and ours compresses lifetimes above six to seven rotations, so we leave the factor-two gap open.

The long-lived spots reported on other stars are measured in a different observable from the features tracked here. The primary spot of GJ 1243 has held its phase for years at a rotation period of 0.59 days (Davenport et al., 2015, 2020). A polar spot on the M4 dwarf TOI-3884 has persisted at least seven years, about 230 rotations, and is invisible to rotational photometry (Libby-Roberts et al., 2023; Tamburo et al., 2025). Vogt and Penrod (1983) put the dissipation time of the great RS CVn spots at 10 to 100 years. Those measurements follow the dominant structure of an individual star, either the large-scale modulation or the main resolved spot group, and neither signal can separate one long-lived spot from serial re-emergence at a fixed site. The features tracked here are individual dips above a measured depth threshold, counted under a tracking ceiling of about 6–7 rotations (Section 3.2), so the 4–7-rotation medians and the coherence over hundreds of rotations describe different objects.

4.3 Outlook

Two limits of the present method, the compression of lifetimes above six rotations and the loss of feature identity on crowded stars, have a common remedy. A likelihood that sums over the possible identities of each dip instead of committing to one set of tracks, fitted through the same forward model of detection, would remove both limits at their common source. Spot-crossing sequences from transits need the same construction before one can treat them as life histories. In a chain built by matching each crossing to the next, false matches between different spots, together with the ceiling on how long the chain can be followed, make spots with a flat hazard appear to age. The same survival analysis applies, through the likelihood of Section 2.3, to the other transient records of stars with published censored life histories: flare sequences, active-region records, and, with that construction, spot-crossing sequences.

A The injection grid of the clock test

We injected spot populations with lifetimes fixed in days, and populations with lifetimes fixed in rotations, into real quiet Kepler light curves and tracked them with the same code that we used on the data. The host light curves were quiet but the injected populations were crowded, with 0.025 births per day, or 0.13 to 0.38 per rotation across the grid. Each spot drifted in phase with a dispersion of 0.02 rotations per rotation and faded linearly after peaking at a quarter of its life, with peak depths drawn from the tracked G–K sample. The fixed-day injections crossed periods of 5–15 d with lifetimes of 15–60 d on a grid of 16 combinations, so the injected lifetimes span 1.0–12.0 rotations and the grid decorrelates the lifetime in days from the lifetime in rotations. The fixed-rotation injections have a lifetime of five rotations at every period, and the recovered lifetime at every grid point is the median over eight simulations. In fitting the slope of recovered lifetime against period we excluded the grid points with injected lifetimes below the visibility limit of 2.5 rotations, because below that limit the recovered lifetimes exceed the injected ones. A second grid extends the periods to 45 d and the fixed lifetimes to 90, 150, and 300 d and to features that never die, with eight simulations per combination and births fixed per day or per rotation. A third builds fixed-day and fixed-rotation populations in the forward model of Section 2.4, on the time sampling, noise, and calibrated crowding of the G–K core stars and of the early-M stars (Sections 3.2 and 3.4).

B Limits of the early-M and fully convective controls

The forward simulations of the matched-sensitivity design (Section 2.5) use modeled noise sampled on the real time grids. On quiet G–K hosts the detection completeness of injections into this modeled noise differs from that of injections into the real light curves by an amount consistent with zero at dip depths of 1,000 ppm and above. On real early-M hosts these differences are unmeasured, so the early-M bounds on aging and the comparison of the two classes rest on a noise model checked only on G–K hosts.

On the fully convective sample, crowding by the stars' own features limits what the injection controls can measure. In a first injection run the tracking preserved the identity of injected features at a rate of 0.467, below the 0.50 we required, because a new feature appears within the matching window before we can score the old one's death. The injected eight-rotation features whose deaths we did recover came back one rotation too long in the median (mean +2.8), because a neighboring feature is captured into the track. Before a second, independent injection run, we required at least 900 of 1,080 injection slots filled (a slot counts as filled when the synthetic feature fits without overlapping the star's own features) and at least 30 of 37 stars with ten or more filled features. The run filled 893 slots on 35 such stars, so we did not take its identity-recovery measurement; its site-recurrence control recovered the injected coincidences at a mean net rate of 0.4295, below the 0.50 required for a recurrence claim on this sample, with rates of 0.3725, 0.4909, 0.3167, 0.5417, and 0.4259 in the five realizations. Simulated populations with no aging on this sample's own time sampling and noise, with birth rates calibrated to its crowding, are a quarter smaller than the real sample and return positive slopes through the same analysis. Their slopes have a median of 0.020 and a 95th percentile of 0.029 per rotation, and their AIC gains a 95th percentile of 42 and a 99th of 59 (300 simulations, Table 2), against −0.0019 and −1.59 for the real sample. Injected aging of solar strength, 0.594 per rotation at the median period, clears that 95th percentile with a positive slope in 27, 14, and 20 of 30 simulated populations for the gradual fade, the abrupt shutdown, and the mixture. At no injected value up to 1.0 per rotation does it do so in 27 or more of 30 for all three profiles. This sample therefore excludes no aging slope up to 1.0 per rotation, solar strength included.

C The solar radial-velocity test

The four analysis configurations of the solar radial-velocity test (Section 3.7) cross a lag window of 1 or 2 days at each whole-rotation lag with covariance-weighted or count-weighted pooling of the four seasons. The five sensitivity variants replace the 200-day running median by 100 or 400 days, the minimum of 10 nightly exposures by 5 or 20, or the running median by a linear detrend per season. We fixed the three reference intervals before analyzing the velocities, one from the quasi-periodic kernel of Klein et al. (2024) and two from the stellar lifetime law. For the kernel we used their fits to the total observed velocity in each of their three seasons. The envelope decay times are 18.0, 21.8, and 21.4 d, the periods 26.37, 27.25, and 27.39 d, and the inverse harmonic complexities 0.22, 0.32, and 0.32. The fourth season of the series analyzed here lies outside their data, and we gave it the third season's values. We varied the decay times and harmonic complexities by their quoted uncertainties and bracketed the harmonic-complexity parameter, the inverse of the values just quoted, between 0.5 and 8, which gives the reference interval $[-1.63, -0.08]$ of Section 3.7. Each interval is the range of T_2 over its model's systematic variants, measured on synthetic series generated on the real observation dates and passed through the same detrending, and widened by two standard errors. The law's two intervals come from a model of active regions whose lifetimes follow the measured distribution, carried to the Sun in days (the days form) or scaled to its rotation period (the rotation form). Such a model predicts T_2 because at whole-rotation lags the autocorrelation envelope does not depend on the visibility kernel of a rotating region or on the mix of flux and convective terms. The kernel interval is negative because the running median that removes the activity cycle leaves a process with no memory beyond a rotation or two, anticorrelated at the second lag. On synthetic series on the same dates, the test classifies a days-form series as the days form in 0.35 of realizations and a rotation-form series as the rotation form in 0.41, because the reference intervals of the two forms lie closer together than the observed interval is wide.

D The fed-site model

The 44-day and 80-day feeding configurations of Figure 5 have the same fixed budget of four members per feature (so the arrival rate is $f = 3/t_f$ for a feeding duration t_f), with members that obey the solar death law. For these two configurations we compare Gompertz slopes of a feature's log hazard against its age in days, computed directly from the model with no detection or tracking step. Figure 5 plots instead the per-rotation slope $\hat{B}$ that the stellar analysis recovers from simulated light curves of the same configurations. When the feeding duration follows an exponential law with mean 44 or 80 days, as in Figure 5, the model's exact hazard law makes the two configurations nearly degenerate in slope, 0.0116 and 0.0118 per day. When it takes the fixed values 44 and 80 days they separate, 0.058 and 0.026 per day, as expected when the feature's termination follows the stopping law of its feeding (Section 3.8). The circles of Figure 5 at 44 and 80 d have median slopes of 0.061 and 0.049 per rotation over their four realizations. The same two configurations with fixed durations, simulated and analyzed in the same way in four realizations each, give 0.102 and 0.070, with ranges that do not overlap (0.089 to 0.112 against 0.062 to 0.077). The full analysis therefore orders them as the exact law does. We did not retune the two fixed-duration configurations to the depth calibration, and their median dip depths are 12 to 18% above and 8 to 15% below its target. We searched a grid of member sizes from the calibrated area down to 1/32 of it, budgets of 4 to 64 members, and feeding durations of 22 to 80 d, exponentially distributed or fixed, together with sustained feeding. We searched the grid for a configuration of solar-law groups whose slope, carried through the measured attenuation of the tracking, falls to the level of the stellar fits. We also required a mean feature lifetime between 3 and 8 rotations and a summed member area within a factor of two of the calibrated one. No configuration on the grid meets all three conditions. The configurations that do reach that level have features living 9 to 14 rotations on average under feeding of finite duration and 9 to 200 rotations under sustained feeding, at depths from 4% to 2.5 times the calibrated one. The single exception inside the lifetime range, sustained feeding by members of 1/32 the calibrated area, has 3% of the calibrated depth.

E Variants of the tracking rules

The G–K result of no detected aging holds under eleven of thirteen sets of tracking rules, the adopted rules and twelve variants (Table A1). It fails only under the two that tighten the phase tolerance for a match from 0.08 to 0.06 rotation. We re-tracked the three samples under twelve variants of the rules of Section 2.2 and refit each with the models of Section 2.3. For every variant we also regenerated, with the same random seeds, eight simulated G–K populations without aging and four with aging injected at $B = 0.05$ (five and five on early M, four and four on the fully convective sample). We tracked them under that variant and refit them, so that each set of rules is judged against its own simulations. Under those eleven, the fitted G–K slope and AIC gain lie below the largest values that the same rules return on their own simulations without aging. Under all thirteen, every G–K population injected at $B = 0.05$ lies above those values. The two exceptions tighten the phase tolerance to 0.06 rotation, with death at the second or the third consecutive miss. There the real slope (0.0209 and 0.0252 per rotation) and gain (30.87 and 43.09) exceed the no-aging maxima (0.0168 and 0.0244, and 15.9 and 39.0). That tolerance breaks 26% of the simulated spots into more than one feature, and 33% of the deaths it records are losses to phase drift, against 19% and 20% under the adopted 0.08. A confirmation rule of three sightings in four rotations raises the real slope to 0.0185, above the percentiles of Table 2. It raises the slopes of that variant's simulations without aging as far (up to 0.0314), which is why each variant needs its own simulations. On the early-M sample the fitted slope lies below every one of the corresponding simulated populations without aging under twelve of the thirteen sets of rules, and on the fully convective sample likewise under twelve. The exception on both is a blend tolerance of 0.10 rotation. On early M the slope then lies inside the range of its five simulations without aging. On the fully convective sample, where that rule censors 69% of the histories, the slope and gain (0.0659 and 75.7) lie above all four of its simulations without aging (at most 0.0468 and 56.9). Under two variants, the wider phase tolerance and the heavier phase weight, the early-M slope is negative (-0.014 and -0.013) and its AIC gain (22.6 and 17.3) exceeds that of every simulation without aging (at most 2.9 and 1.7). Under those two variants the fitted early-M hazard therefore declines with age instead of staying flat. The completed median lifetimes stay between 4 and 6 rotations on both Kepler samples and between 4 and 8 on the fully convective sample. There death at the third miss, a wider tolerance, or a stricter confirmation rule lengthens the tracked lifetimes by up to three rotations. The days-versus-period slope of the G–K core sample stays between 0.74 and 0.99 across the variants (standard errors 0.13 to 0.17), within two standard errors of each variant's own fixed-rotation injections under all thirteen sets of rules. Under the nine sets of rules that keep the phase tolerance at 0.08 it stays three or more standard errors above the variant's fixed-day injections, and under the four that change the tolerance, 2.3 to 3.7.

Table A1: Survival fit of the G–K core sample re-tracked under variants of the tracking rules of Section 2.2. The first row is the adopted set of rules of Section 2.2. Those are a phase tolerance of 0.08 rotation, death at the second consecutive observed rotation without a matching dip, confirmation by two sightings within three rotations, phase weight $\alpha = 0.3$, and blend censoring below a separation of 0.06 rotation. Each other row changes only the rules named. Stars, features, and median life are the stars with at least ten tracked features under those rules, the features they carry into the fit, and the median completed lifetime in rotations, as in Table 2. Beside each row's fitted slope $\hat{B}$ and AIC gain ΔAIC, the table lists the largest values of both over eight simulated populations without aging, regenerated and tracked under the same rules. It also lists the smallest slope over four populations injected with $B = 0.05$. The eight populations without aging are fewer than the 300 of Table 2, so their maxima are not the 95th percentiles quoted there. In every row except the two with tolerance 0.06 the real slope and gain lie below the no-aging maxima, and in every row the smallest $B = 0.05$ slope lies above the largest no-aging slope.

Rules	Stars	Features	Med. life [rot]	$\hat{B}$	no-aging, max $\hat{B}$	$B = 0.05$, min $\hat{B}$	ΔAIC	no-aging, max ΔAIC
Adopted rules	89	1,988	5.0	+0.0056	0.0127	0.0227	1.17	10.0
Phase tolerance 0.06	95	2,532	4.0	+0.0209	0.0168	0.0194	30.87	15.9
Phase tolerance 0.10	83	1,611	6.0	−0.0028	0.0132	0.0222	−1.06	10.6
Death at third miss	86	1,778	5.0	+0.0082	0.0197	0.0299	5.21	28.7
Tolerance 0.06, death at third miss	94	2,396	4.0	+0.0252	0.0244	0.0248	43.09	39.0
Tolerance 0.10, death at third miss	77	1,405	6.0	+0.0008	0.0151	0.0229	−1.92	15.5
Confirmation 2 in 4 rotations	89	2,024	5.0	+0.0014	0.0127	0.0223	−1.75	10.2
Phase weight $\alpha = 0.5$	84	1,764	5.0	−0.0034	0.0099	0.0172	−0.65	5.7
Confirmation 2 in 2 rotations	81	1,630	5.0	+0.0086	0.0131	0.0221	3.72	9.3
Confirmation 3 in 4 rotations	75	1,330	6.0	+0.0185	0.0314	0.0394	26.35	54.6
No blend censoring	89	1,948	5.0	+0.0051	0.0129	0.0230	0.69	10.9
Blend tolerance 0.10	90	2,089	5.0	+0.0056	0.0139	0.0237	0.79	11.1
Blended histories dropped	89	1,877	5.0	+0.0042	0.0123	0.0219	−0.20	9.4

F Machine-readable tables

Two machine-readable tables accompany this paper, one with a row per star and one with a row per tracked feature, and we leave a cell empty where the quantity is not available. The star table has 516 rows, the 249 G–K, 230 early-M, and 37 fully convective stars of Table 1, of which 509 have tracked features, each row listing the identifier, the stellar parameters, the rotation period and its source, the numbers of tracked features, deaths, censored histories, and observed rotation cycles, the median completed lifetime, and the subsample flags (Section 2.1). The feature table has 10,051 rows, the 4,954 G–K, 2,875 early-M, and 2,222 fully convective features, each with birth epoch, age at last match and death interval, duration, event and censoring type, depth at birth and at peak, sightings, and the site-recurrence pairing of Section 2.2. A supplementary pair of tables lists, in the same columns, the 8 stars of the G–K core sample that lie outside the 249-star selection, all of which enter the pooled fit of Table 2, and their 158 features. With the tables we release the three target lists with their selection quantities, the detection and tracking constants of Section 2.2, and the injection grids, tracking-rule variants, and random seeds of Sections 2.4 and 3.2 and Appendices A and E. We also release the nest-linking rules of Section 3.8 and the survival-fit and simulation code.

References

G. Basri and H. T. Nguyen. Double-dipping: A new relation between stellar rotation and starspot activity. *The Astrophysical Journal*, 863:190, 2018. doi: 10.3847/1538-4357/aad3b6. arXiv:1805.04587.

Gibor Basri, Tristan Streichenberger, Connor McWard, Lawrence Edmond, IV, Joanne Tan, Minjoo Lee, and Trey Melton. A new method for estimating starspot lifetimes based on autocorrelation functions. *The Astrophysical Journal*, 924:31, 2022. doi: 10.3847/1538-4357/ac3420. arXiv:2110.13284.

S. J. Bradshaw and P. Hartigan. On sunspot and starspot lifetimes. *The Astrophysical Journal*, 795: 79, 2014. doi: 10.1088/0004-637X/795/1/79. arXiv:1409.4337.

M. J. M. Castenmiller, C. Zwaan, and E. B. J. van der Zalm. Sunspot nests: Manifestations of sequences in magnetic activity. *Solar Physics*, 105:237–255, 1986.

D. R. Cox. Regression models and life-tables. *Journal of the Royal Statistical Society: Series B (Methodological)*, 34(2):187–202, 1972. doi: 10.1111/j.2517-6161.1972.tb00899.x.

S. R. Cranmer and S. H. Saar. Testing a predictive theoretical model for the mass loss rates of cool stars. *The Astrophysical Journal*, 741:54, 2011.

James R. A. Davenport, Leslie Hebb, and Suzanne L. Hawley. Detecting differential rotation and starspot evolution on the M dwarf GJ 1243 with Kepler. *The Astrophysical Journal*, 806:212, 2015. doi: 10.1088/0004-637X/806/2/212. arXiv:1505.01524.

James R. A. Davenport, Guadalupe Tovar Mendoza, and Suzanne L. Hawley. 10 years of stellar activity for GJ 1243. *The Astronomical Journal*, 160:36, 2020. doi: 10.3847/1538-3881/ab9536. arXiv:2005.10281.

L. Degott, F. Baudin, R. Samadi, B. Perri, and C. Pinçon. Activity of low-mass stars in the light of spot signature in the Fourier domain. *Astronomy & Astrophysics*, 696:A41, 2025. doi: 10.1051/0004-6361/202451205. arXiv:2502.15329.

X. Dumusque, N. C. Santos, S. Udry, C. Lovis, and X. Bonfils. Planetary detection limits taking into account stellar noise. II. effect of stellar spot groups on radial-velocities. *Astronomy & Astrophysics*, 527:A82, 2011. doi: 10.1051/0004-6361/201015877. arXiv:1101.0954.

X. Dumusque, K. Al Moulla, M. Cretignier, N. Buchschacher, D. Segransan, D. F. Phillips, L. Affer, S. Aigrain, A. Anna John, A. S. Bonomo, V. Bourrier, L. A. Buchhave, A. Collier Cameron, H. M. Cegla, P. Cortés-Zuleta, R. Cosentino, J. Costes, M. Damasso, Z. L. de Beurs, D. Ehrenreich, A. Ghedina, M. Gonzales, R. D. Haywood, B. Klein, B. S. Lakeland, N. Langellier, D. W. Latham, A. Leleu, M. Lodi, M. Lopez-Morales, C. Lovis, L. Malavolta, J. Maldonado, G. Mantovan, A. F. Matínez Fiorenzano, G. Micela, T. Milbourne, E. Molinari, A. Mortier, L. Naponiello, B. A. Nicholson, N. K. O'Sullivan, F. Pepe, M. Pinamonti, G. Piotto, F. Rescigno, K. Rice, S. Dimitar, A. M. Silva, A. Sozzetti, M. Stalport, S. Tavella, S. Udry, A. Vanderburg, S. Vissapragada, and C. A. Watson. A decade of solar high-fidelity spectroscopy and precise radial velocities from HARPS-N. *Astronomy & Astrophysics*, 706:A231, 2026. doi: 10.1051/0004-6361/202557132. arXiv:2510.27635.

E. D. Feigelson and P. I. Nelson. Statistical methods for astronomical data with upper limits. I. Univariate distributions. *The Astrophysical Journal*, 293:192, 1985. doi: 10.1086/163225.

H. A. C. Giles, A. Collier Cameron, and R. D. Haywood. A Kepler study of starspot lifetimes with respect to light curve amplitude and spectral type. *Monthly Notices of the Royal Astronomical Society*, 472:1618–1627, 2017. doi: 10.1093/mnras/stx1931. arXiv:1707.08583.

S. Gossage, R. Kiman, K. Monsch, A. A. Medina, J. J. Drake, C. Garraffo, Y. Lu, J. D. Wing, and N. J. Wright. On convective turnover times and dynamos in low-mass stars. *The Astrophysical Journal*, 988:102, 2025. doi: 10.3847/1538-4357/adde4d. arXiv:2410.20000.

Douglas S. Hall and Michael R. Busby. Starspot lifetimes. In *Active Close Binaries*, volume 319 of *NATO ASI Series C*, pages 377–392. Springer Netherlands, Dordrecht, 1990. doi: 10.1007/978-94-009-0679-2_30.

Douglas S. Hall and Gregory W. Henry. The law of starspot lifetimes. *I.A.P.P.P. Communications*, 55:51–57, 1994.

R. D. Haywood, A. Collier Cameron, D. Queloz, S. C. C. Barros, M. Deleuil, R. Fares, M. Gillon, A. F. Lanza, C. Lovis, C. Moutou, F. Pepe, D. Pollacco, A. Santerne, D. Ségransan, and Y. C. Unruh. Planets and stellar activity: hide and seek in the CoRoT-7 system. *Monthly Notices of the Royal Astronomical Society*, 443:2517, 2014. doi: 10.1093/mnras/stu1320. arXiv:1407.1044.

R. D. Haywood, A. Collier Cameron, Y. C. Unruh, C. Lovis, A. F. Lanza, J. Llama, M. Deleuil, R. Fares, M. Gillon, C. Moutou, F. Pepe, D. Pollacco, D. Queloz, and D. Ségransan. The Sun as a planet-host star: proxies from SDO images for HARPS radial-velocity variations. *Monthly Notices of the Royal Astronomical Society*, 457:3637, 2016. doi: 10.1093/mnras/stw187. arXiv:1601.05651.

E. Işık, A. Valio, A. Strugarek, S. Järvinen, K. Vida, A. Buccino, K. Namekata, T. Hackman, J. Alvarado-Gomez, D. Nandy, A. O. Farrish, K. Poppenhäger, and P. Figueira. Magnetic activity in cool stars: manifestations and relevance to exoplanets. *arXiv e-prints*, 2026. arXiv:2606.31617.

E. L. Kaplan and Paul Meier. Nonparametric estimation from incomplete observations. *Journal of the American Statistical Association*, 53(282):457–481, 1958. doi: 10.1080/01621459.1958.10501452.

Baptiste Klein, Suzanne Aigrain, Michael Cretignier, Khaled Al Moulla, Xavier Dumusque, Oscar Barragán, Haochuan Yu, Annelies Mortier, Federica Rescigno, Andrew Collier Cameron, Mercedes López-Morales, Nadège Meunier, Alessandro Sozzetti, and Niamh K. O'Sullivan. Investigating stellar activity through eight years of Sun-as-a-star observations. *Monthly Notices of the Royal Astronomical Society*, 531:4238, 2024. doi: 10.1093/mnras/stae1313. arXiv:2405.12065.

Greg Kopp. Magnitudes and timescales of total solar irradiance variability. *Journal of Space Weather and Space Climate*, 6:A30, 2016. doi: 10.1051/swsc/2016025. arXiv:1606.05258.

Jessica E. Libby-Roberts, Maria Schutte, Leslie Hebb, et al. An in-depth look at TOI-3884b: A super-Neptune transiting an M4 dwarf with persistent starspot crossings. *The Astronomical Journal*, 165:249, 2023. doi: 10.3847/1538-3881/accc2f.

V. Martínez Pillet, F. Moreno-Insertis, and M. Vázquez. The distribution of sunspot decay rates. *Astronomy & Astrophysics*, 274:521–533, 1993.

S. Mathur, D. Huber, N. M. Batalha, D. R. Ciardi, F. A. Bastien, A. Bieryla, L. A. Buchhave, W. D. Cochran, M. Endl, G. A. Esquerdo, E. Furlan, A. W. Howard, S. B. Howell, H. Isaacson, D. W. Latham, P. J. MacQueen, and D. R. Silva. Revised stellar properties of Kepler targets for the Q1-17 (DR25) transit detection run. *The Astrophysical Journal Supplement Series*, 229:30, 2017. doi: 10.3847/1538-4365/229/2/30. arXiv:1609.04128.

A. McQuillan, T. Mazeh, and S. Aigrain. Rotation periods of 34,030 Kepler main-sequence stars: The full autocorrelation sample. *The Astrophysical Journal Supplement Series*, 211:24, 2014.

Kosuke Namekata, Hiroyuki Maehara, Yuta Notsu, Shin Toriumi, Hisashi Hayakawa, Kai Ikuta, Shota Notsu, Satoshi Honda, Daisaku Nogami, and Kazunari Shibata. Lifetimes and emergence/decay rates of star spots on solar-type stars estimated by Kepler data in comparison with those of sunspots. *The Astrophysical Journal*, 871:187, 2019. doi: 10.3847/1538-4357/aaf471. arXiv:1811.10782.

Kosuke Namekata, James R. A. Davenport, Brett M. Morris, Suzanne L. Hawley, Hiroyuki Maehara, Yuta Notsu, Shin Toriumi, Kai Ikuta, Shota Notsu, Satoshi Honda, Daisaku Nogami, and Kazunari Shibata. Temporal evolution of spatially resolved individual star spots on a planet-hosting solar-type star: Kepler-17. *The Astrophysical Journal*, 891:103, 2020. doi: 10.3847/1538-4357/ab7384. arXiv:2002.01086.

N.-E. Nèmec, A. I. Shapiro, E. Işık, S. K. Solanki, and T. Reinhold. Forward modelling of brightness variations in Sun-like stars. II. Light curves and variability. *Astronomy & Astrophysics*, 672:A138, 2023. doi: 10.1051/0004-6361/202244412. arXiv:2303.03040.

A. A. Norton, A. Mendez, R. Chen, M. Dikpati, and S. Aswin Amirtha Raj. Moderate nesting and cross-equatorial asymmetry of active regions in Solar Cycle 24. *Journal of Astrophysics and Astronomy*, 47:48, 2026. doi: 10.1007/s12036-026-10157-0. arXiv:2511.03646.

R. W. Noyes, L. W. Hartmann, S. L. Baliunas, D. K. Duncan, and A. H. Vaughan. Rotation, convection, and magnetic activity in lower main-sequence stars. *The Astrophysical Journal*, 279: 763–777, 1984.

K. Petrovay and L. van Driel-Gesztelyi. Making sense of sunspot decay. I. Parabolic decay law and Gnevyshev–Waldmeier relation. *Solar Physics*, 176:249–266, 1997. doi: 10.1023/A:1004988123265. arXiv:astro-ph/9706029.

V. Rajpaul, S. Aigrain, M. A. Osborne, S. Reece, and S. Roberts. A Gaussian process framework for modelling stellar activity signals in radial velocity data. *Monthly Notices of the Royal Astronomical Society*, 452:2269, 2015. doi: 10.1093/mnras/stv1428. arXiv:1506.07304.

G. R. Ricker et al. Transiting exoplanet survey satellite. *Journal of Astronomical Telescopes, Instruments, and Systems*, 1:014003, 2015. doi: 10.1117/1.JATIS.1.1.014003. arXiv:1406.0151.

A. R. G. Santos, S. Mathur, R. A. García, M. S. Cunha, and P. P. Avelino. On the relation between active-region lifetimes and the autocorrelation function of light curves. *Monthly Notices of the Royal Astronomical Society*, 508:267–278, 2021. doi: 10.1093/mnras/stab2402. arXiv:2108.08616.

M. D. Schwartz and C. Garraffo. Demography of sunspots: aging and death by turbulent erosion. Paper I, in preparation, 2026.

A. Skumanich. Time scales for Ca II emission decay, rotational braking, and lithium depletion. *The Astrophysical Journal*, 171:565, 1972.

K. Sowmya, N.-E. Nèmec, A. I. Shapiro, E. Işık, N. A. Krivova, and S. K. Solanki. Predictions of astrometric jitter for Sun-like stars. III. Fast rotators. *The Astrophysical Journal*, 934:146, 2022. doi: 10.3847/1538-4357/ac79b3.

K. G. Stassun et al. The revised TESS input catalog and candidate target list. *The Astronomical Journal*, 158:138, 2019. doi: 10.3847/1538-3881/ab3467. arXiv:1905.10694.

Patrick Tamburo, Samuel W. Yee, Juliana García-Mejía, David Charbonneau, Allyson Bieryla, Karen A. Collins, and Avi Shporer. Spot-crossing variations confirm a misaligned orbit for a planet transiting an M dwarf. *arXiv e-prints*, 2025. arXiv:2506.11998.

Takato Tokuno, Kosuke Namekata, Hiroyuki Maehara, and Shin Toriumi. Temporal variation of flare occurrence rates via the spot evolution on the Sun and solar-type stars. *The Astrophysical Journal*, 985:158, 2025. doi: 10.3847/1538-4357/adce7c. arXiv:2504.12761.

Shin Toriumi, Vladimir S. Airapetian, Hugh S. Hudson, Carolus J. Schrijver, Mark C. M. Cheung, and Marc L. DeRosa. Sun-as-a-star spectral irradiance observations of transiting active regions. *The Astrophysical Journal*, 902:36, 2020. doi: 10.3847/1538-4357/abadf9. arXiv:2008.04319.

S. S. Vogt and G. D. Penrod. Doppler imaging of spotted stars - application to the RS Canum Venaticorum star HR 1099. *Publications of the Astronomical Society of the Pacific*, 95:565, 1983. doi: 10.1086/131208.

N. J. Wright and J. J. Drake. Solar-type dynamo behaviour in fully convective stars without a tachocline. *Nature*, 535:526–528, 2016.

N. J. Wright, J. J. Drake, E. E. Mamajek, and G. W. Henry. The stellar-activity–rotation relationship and the evolution of stellar dynamos. *The Astrophysical Journal*, 743:48, 2011.

N. J. Wright, E. R. Newton, P. K. G. Williams, J. J. Drake, and R. K. Yadav. The stellar rotation–activity relationship in fully convective M dwarfs. *Monthly Notices of the Royal Astronomical Society*, 479:2351–2360, 2018.

Junwei Zhao, Ruizhu Chen, and Aimee A. Norton. Long-term clustering pattern of solar active regions and their potential connection with magneto-Rossby waves. *The Astrophysical Journal*, 1004:175, 2026. doi: 10.3847/1538-4357/ae734d. arXiv:2605.25501.